



# Linked and fully-coupled 3D earthquake dynamic rupture and tsunami modeling for the Húsavík-Flatey Fault Zone in North Iceland

Fabian Kutschera<sup>1</sup>, Alice-Agnes Gabriel<sup>2,1</sup>, Sara Aniko Wirp<sup>1</sup>, Bo Li<sup>3,1</sup>, Thomas Ulrich<sup>1</sup>, Claudia Abril<sup>4</sup>, and Benedikt Halldórsson<sup>5,6</sup>

<sup>1</sup>Institute of Geophysics, Department of Earth and Environmental Sciences, Ludwig-Maximilians-University, Munich, Germany

<sup>2</sup>Institute of Geophysics and Planetary Physics, Scripps Institution of Oceanography, UC San Diego, California, USA

<sup>3</sup>Division of Physical Sciences and Engineering, King Abdullah University of Science and Technology, Thuwal, Saudi Arabia

<sup>4</sup>Department of Earth Sciences, Uppsala University, Sweden

<sup>5</sup>Division of Processing and Research, Icelandic Meteorological Office, Reykjavík, Iceland

<sup>6</sup>Faculty of Civil and Environmental Engineering, School of Engineering and Natural Sciences, University of Iceland, Reykjavík, Iceland

**Correspondence:** Fabian Kutschera (fabian.kutschera@geophysik.uni-muenchen.de)

## Abstract.

Tsunamigenic earthquakes pose considerable risks, both economically and socially, yet earthquake and tsunami hazard assessments are typically conducted separately. Earthquakes associated with unexpected tsunamis, such as the 2018  $M_W$  7.5 strike-slip Sulawesi earthquake, emphasize the need to study the tsunami potential of active submarine faults in different tectonic settings. Here, we investigate physics-based scenarios combining 3D earthquake dynamic rupture with tsunami generation and propagation for the  $\sim 100$  km long Húsavík-Flatey Fault Zone in North Iceland using time-dependent one-way linked and 3D fully-coupled earthquake-tsunami modeling. Our analysis shows that the HFFZ has the potential to generate sizeable tsunamis. The six dynamic rupture models sourcing our tsunami scenarios vary regarding hypocenter location, spatio-temporal evolution, fault slip, and fault structure complexity but coincide with historical earthquake magnitudes. We find that the earthquake dynamic rupture scenarios on a less segmented fault system, particularly with a hypocenter location in the eastern part of the fault system, have a larger potential for local tsunami generation. Here, dynamically evolving large shallow fault slip ( $\sim 8$  m), near-surface rake rotation ( $\pm 20^\circ$ ), and significant coseismic vertical displacements of the local bathymetry ( $\pm 1$  m) facilitate strike-slip faulting tsunami generation. We model tsunami crest-to-trough differences (total wave heights) of up to  $\sim 0.9$  m near the town Ólafsfjörður. In contrast, none of our scenarios endanger the town of Akureyri, which is shielded by multiple reflections within the narrow Eyjafjörður Bay and by Hrísey Island.

We compare the modeled one-way linked tsunami waveforms with simulation results using a 3D fully-coupled approach. We find good agreement in the tsunami arrival times and location of maximum tsunami heights. While seismic waves result in transient motions of the sea surface and affect the ocean response, they do not appear to contribute to tsunami generation. However, complex source effects arise in the fully-coupled simulations, such as tsunami dispersion effects and complex superposition of seismic and acoustic waves within the shallow continental shelf of North Iceland. We find that the vertical velocities



of near-source acoustic waves are unexpectedly high - larger than those corresponding to the actual tsunami - which may serve as a rapid indicator of surface dynamic rupture. Our results have important implications for understanding the tsunamigenic potential of strike-slip fault systems worldwide and the co-seismic acoustic wave excitation during tsunami generation and may help to inform future tsunami early warning systems.

## 25 **1 Introduction**

Earthquake-generated tsunamis are generally associated with large submarine events on dip-slip faults, in particular at subduction zone megathrust interfaces (e.g., Bilek and Lay, 2018; Lotto et al., 2018; Melgar and Ruiz-Angulo, 2018; Wirp et al., 2021). The potential generation of a tsunami depends not only on the magnitude of the earthquake, but on the rupture process (e.g., Kanamori, 1972; Ulrich et al., 2022), the geomorphology of the region (e.g., Mori et al., 2022) and secondary effects  
30 such as landsliding or mass slumping (Harbitz et al., 2006; Løvholt et al., 2015; Moretti et al., 2020; Poulain et al., 2022). The typically underrepresented tsunami hazard posed by large (partially) submarine strike-slip fault systems has received increasing attention since the unexpected and devastating local tsunami in Palu Bay following the 2018  $M_W$  7.5 strike-slip Sulawesi earthquake in Indonesia (Ulrich et al., 2019b; Bao et al., 2019; Socquet et al., 2019; Elbanna et al., 2021; Amlani et al., 2022; Ma, 2022). Assessing the tsunamigenic potential of strike-slip fault systems has important implications worldwide, such as for  
35 the Dead Sea Transform fault system, the Enriquillo–Plantain Garden fault zone in Haiti, and for Northern offshore sections of the San Andreas Fault in California.

Here, we focus on the  $\sim$ 100 km long Húsavík-Flatey Fault Zone (HFFZ), the largest strike-slip fault in Iceland, which is part of the Tjörnes Fracture Zone (TFZ). The TFZ is a complex transcurrent fault system and links the Kolbeinsey Ridge (KR) as part of the Mid-Atlantic Ridge offshore North of Iceland (Eyjafjarðaráll Rift Zone) to its manifestation on land in the Northern  
40 Volcanic Zone (NVZ), which is characterized by volcanic systems and extensional faulting (Sæmundsson, 1974; Einarsson, 1991; Geirsson et al., 2006; Einarsson, 2008; Stefansson et al., 2008; Einarsson and Brandsdóttir, 2021). Earthquake faulting in the TFZ is driven by eastward spreading of the Eurasian Plate with an average velocity of  $\sim$ 18 mm/yr relative to the North American Plate (Demets et al., 2010). The HFFZ strikes from offshore to onshore and is characterized by right-lateral (dextral) strike-slip faulting, a faulting mechanism which appears frequently subparallel to the adjacent active rift zones of Iceland  
45 (Karson et al., 2018). The HFFZ is one of three main faulting lineaments that form the majority of earthquake faulting in the TFZ. It poses the largest threat to coastline communities such as the town of Húsavík, which is located atop the Húsavík-Flatey Fault Zone at the eastern side of Skjálíandi Bay.

The region of Norðurland eystra has experienced several large earthquakes in the past. Two magnitude 6.5 earthquakes occurred in 1872 and a recent  $M_W$  6 earthquake struck the western end of the HFFZ in 2020 (Fig. 1). The strongest historically  
50 recorded  $M$  7 event in 1755 caused extensive damage and may have generated a series of oceanic waves (i.e., a tsunami) that hit the coastline (Stefansson et al., 2008; Þorgeirsson, 2011; Ruiz-Angulo et al., 2019). High-resolution seismic reflection data within Skjálíandi Bay reveal up to 15 m of accumulated vertical offset since the last glacial maximum (Magnúsdóttir et al., 2015; Brandsdóttir et al., 2022), indicating possible vertical deformation of the ocean bottom during past earthquakes. This



emphasizes the relevance of studying the Húsavík-Flatey Fault Zone from earthquake rupture to its tsunami potential. Metzger and Jónsson (2014) estimate that 30 % to 50 % of the full transform motion is taken up by the HFFZ, corresponding to a geodetic slip rate of 6 to 9 mm yr<sup>-1</sup>. Thus, a locked HFFZ may host potential  $M_W$  6.8 ± 0.1 earthquakes (Metzger et al., 2011, 2013). Although the long-term Holocene slip rate is presumably slower than the present-day geodetic slip rate, it can be used to derive an average recurrence time of 500 years for a  $M_W$  7 earthquake on the HFFZ (Matrau et al., 2022). De Pascale (2022) calculate a recurrence interval of 32±24 for a magnitude 6 event. Recent GNSS-derived velocities, using more than 100 continuous and campaign-style GPS stations in total, are close to zero near the fault, indicating that the HFFZ may be fully locked (Barreto et al., 2022).

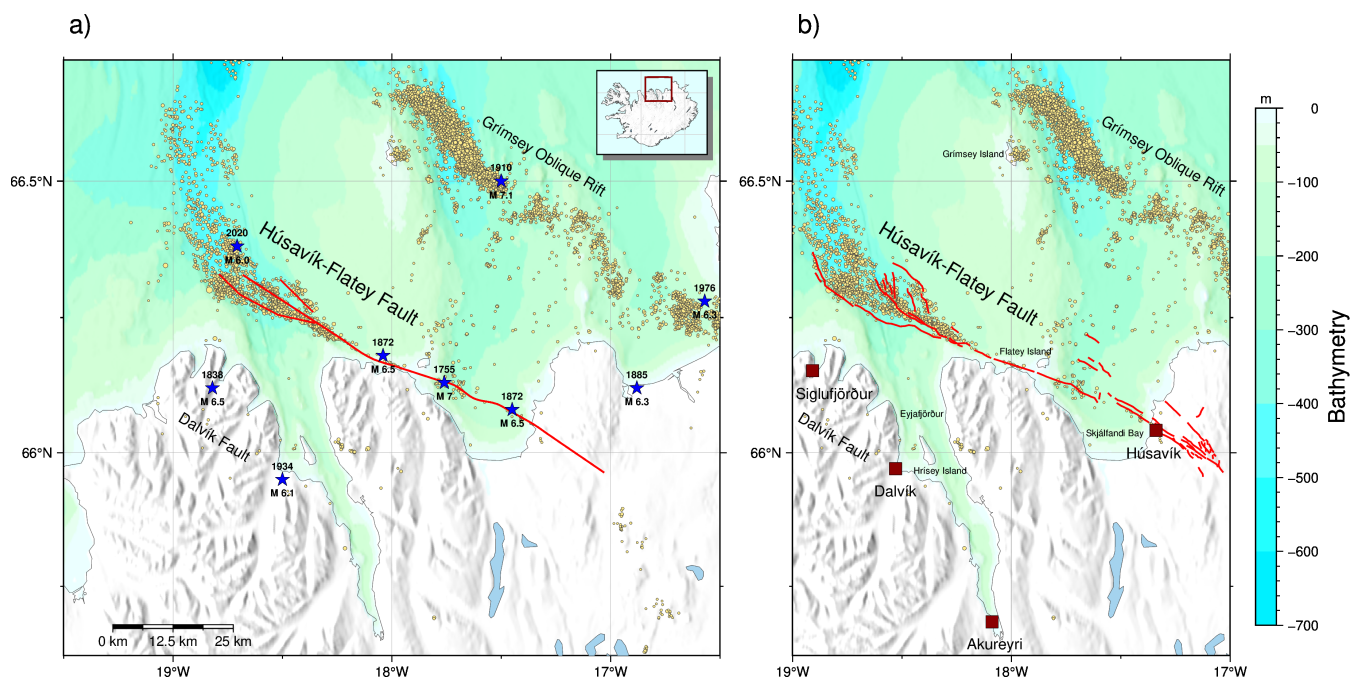


**Figure 1.** Overview of the Tjörnes Fracture Zone (TFZ). Yellow circles represent relocated seismicity from 1993 to 2019 (Abril et al., 2018, 2019). a) The here used “simple” fault geometry of the Húsavík-Flatey Fault Zone (HFFZ), which has three segments, is shown as red lines (Li et al., 2023). Historic large earthquakes with  $M \geq 6$  are indicated as blue stars (Ambraseys and Sigbjörnsson, 2000; Stefansson et al., 2008; Þorgeirsson, 2011; Jónsson, 2019). b) The used “complex” fault geometry of the HFFZ (Li et al., 2023), which includes 55 fault segments (shown as red lines) together with major towns in the region of Norðurland eystra.

A better understanding of the complex interaction between static and time-dependent earthquake displacements, off-fault deformation, and seismic, acoustic, and tsunami amplitudes is now possible using realistic 3D scenarios. Non-linear earthquake dynamic rupture simulations combining coseismic frictional failure on prescribed faults and seismic wave propagation are powerful tools to investigate earthquake dynamics as a consequence of the model’s initial conditions (e.g., Aochi and Ulrich, 2015; Wollherr et al., 2019; Ulrich et al., 2019a; Lozos and Harris, 2020; Harris et al., 2021; Taufiqurrahman et al., 2022; Biemiller



et al., 2023). Empowered by high-performance computing (Ben-Zion et al., 2022), joint earthquake-tsunami modeling is now becoming applicable for the development of (probabilistic) tsunami forecasting and early warning systems (Yamamoto, 1982; Cecioni et al., 2014; Bernard and Titov, 2015; Mei and Kadri, 2017; Gomez and Kadri, 2021; Selva et al., 2021). In this study, we investigate the tsunami potential of the HFFZ using both one-way linked 3D earthquake dynamic rupture and shallow-water equations tsunami simulations (Ulrich et al., 2019b; Madden et al., 2020; Wirp et al., 2021; Ulrich et al., 2022; van Zelst et al., 2022), and 3D fully-coupled elastic-acoustic earthquake-tsunami simulations (Krenz et al., 2021; Abrahams et al., 2023). We use six different dynamic rupture scenarios (Fig. 2) from a suite of recently developed physics-based dynamic rupture models (Li et al., 2023), which were simulated using SeisSol, a scientific open-source software for 3D earthquake dynamic rupture simulations. The chosen dynamic rupture models vary in their hypocenter location, spatio-temporal evolution of rupture dynamics, fault slip, and geometric fault system complexity. They coincide with historically and physically plausible earthquake magnitudes, stress drop, rupture speed, and slip distributions (Li et al., 2023), and produce ground motions that have been verified against empirical Ground Motion Models (GMMs) calibrated for Iceland (Kowsari et al., 2020). Our one-way linked earthquake-tsunami scenarios use the simulated time-dependent bathymetry displacements as a forcing term for a non-linear shallow water solver. The fully-coupled method captures 3D earthquake rupture, seismic, and acoustic wave propagation in the Earth and the ocean, as well as tsunami wave generation and propagation.

We detail the earthquake and tsunami model setups in Sect. 2. Sect. 3.1 summarizes the six dynamic rupture earthquake scenarios. In Sect. 3.2.1 we investigate physically plausible scenarios of potentially tsunamigenic HFFZ earthquakes by using the one-way linked earthquake-tsunami modeling approach for all six dynamic rupture scenarios. We show that the HFFZ may generate tsunamigenic earthquakes, potentially posing a significant hazard to coastline communities. Based on the results from the one-way linked simulations, we select the three earthquake-tsunami scenarios on the simpler fault geometry causing larger wave heights for the fully-coupled approach to better understand the initial tsunami genesis and complex superposition of seismic, acoustic, and tsunami waves. We compare the results for both earthquake-tsunami modeling techniques in Sect. 3.2.2.

## 2 Model setup

We model one-way linked (cf. Sect. 2.4) and fully-coupled (cf. Sect. 2.5) tsunami scenarios (Abrahams et al., 2023) that are sourced by earthquakes simulated as dynamically propagating shear rupture (Ramos et al., 2022) on seismically locked (Wang and Dixon, 2004) pre-existing faults.

We use six earthquake scenarios based on a suite of 3D spontaneous dynamic rupture simulations developed in Li et al. (2023) that can match local GMMs and reproduce historic earthquake magnitudes. Dynamic rupture modeling includes solving for the spontaneous frictional failure non-linearly linked to the propagation of seismic waves (Fig. 3) with the purpose of gaining knowledge about the underlying physical processes. Such physically self-consistent descriptions of how faults yield and slide have been developed for complex and/or poorly instrumented earthquakes in various tectonic contexts (e.g., Olsen et al., 1997; Douilly et al., 2015; Kyriakopoulos et al., 2017; Harris et al., 2021; Taufiqurrahman et al., 2023). In contrast to kinematic earthquake source modeling, fault slip is not prescribed, but the rupture dynamics evolve based on an empirical friction law



100 and chosen initial conditions. Here, the dynamic rupture initial conditions (including fault geometries, pre-stress, and strength) are constrained by seismic, geodetic, and bathymetry observations as briefly summarized in the following sections. For details and sensitivity analysis of HFFZ dynamic rupture simulations and their initial conditions we refer to Li et al. (2023).

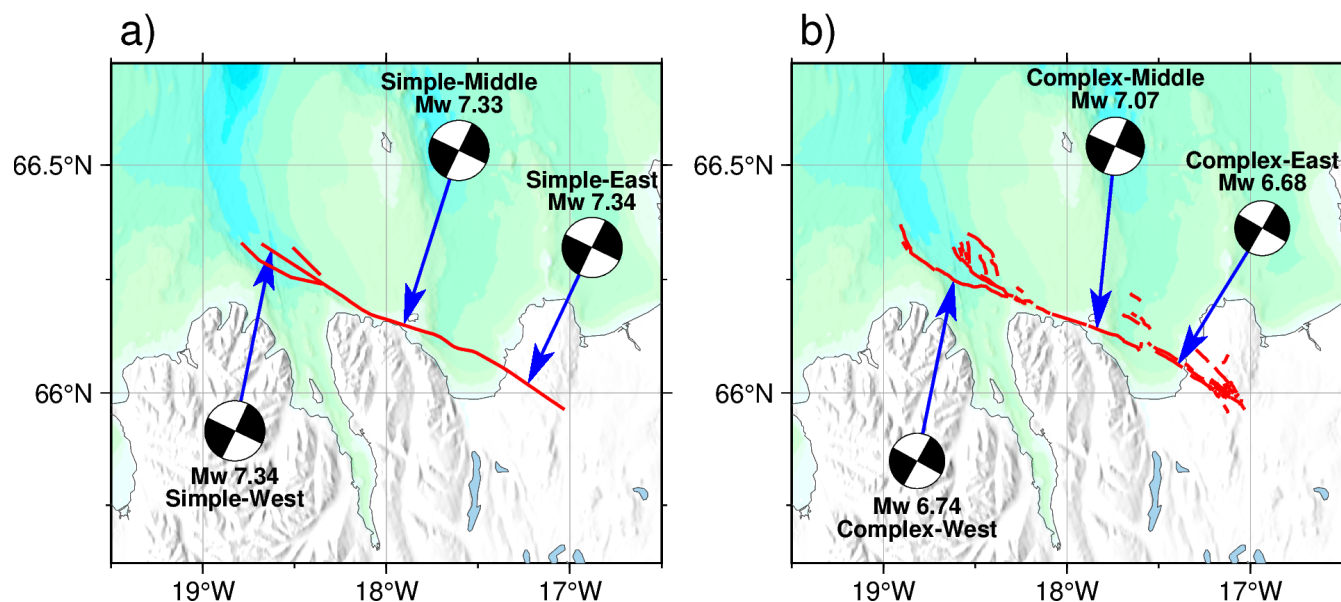


**Figure 2.** Overview over the six 3D dynamic rupture earthquake scenarios based on Li et al. (2023). Arrows indicate the three varied epicenter locations. Each dynamic rupture scenario is nucleated at a hypocentral depth of 7 km. We show the on-fault measured moment magnitude and the equivalent centroid moment tensor solutions (constructed after Ulrich et al. (2022)) representing overall strike-slip faulting mechanisms of the dynamic rupture scenarios. a) shows the three dynamic rupture models on the simple fault system geometry with varying epicentral locations and b) are the three scenarios on the complex fault system geometry.

## 2.1 Fault geometry and subsurface structure

The fault geometry of active submarine fault systems plays an important role in the potential for tsunami generation caused by earthquake rupture. Fault trenching has been conducted for the onshore part of the HFFZ (Harrington et al., 2016; Matrau et al., 2021) and can be used to extrapolate the location of the off-shore fault trace. Recent offshore seismic reflection campaigns in North Iceland and high-resolution bathymetry interpretation (Brandsdóttir et al., 2005; Magnúsdóttir and Brandsdóttir, 2011; Magnúsdóttir et al., 2015; Hjartardóttir et al., 2016) together with relocated seismicity (Abril et al., 2018, 2019) provide detailed insight on the complex off-shore fault system structure. However, it remains challenging to decide which degree of fault system complexity is important for tsunami hazards and to gain direct constraints on the variability of the off-shore geometry of the HFFZ fault system. To capture some of the geometric uncertainty, we consider two proposed fault geometries (Fig. 1, 2) with varying degrees of complexity. The complex fault geometry comprises 55 partially cross-cutting fault segments, each vertically dipping and intersecting with the complex geomorphology (Li et al., 2023). The simpler fault geometry is



115 composed of one main fault segment with two shorter adjoint fault segments in the West. We assume vertical fault segments that agree with relocated seismicity (Abril et al., 2018, 2019). All faults are embedded in the same recent 3D velocity model (Abril et al., 2021). We subsequently refer to the three earthquake dynamic rupture scenarios on the simpler fault geometry as “Simple-West”, “Simple-Middle” and “Simple-East”, while the three models on the highly complex fault geometry are called “Complex-West”, “Complex-Middle” and “Complex-East” – the cardinal directions correspond to the epicenter locations with respect to the fault systems as shown in Fig. 2.

## 120 2.2 Initial stresses and fault friction parametrization

Following Ulrich et al. (2019a), Li et al. (2023) combine Anderson’s theory of faulting in combination with Mohr-Coulomb theory of frictional failure (Coulomb, 1776; Anderson, 1905; C  l  rier, 2008) to define realistic levels of prestress for all dynamic rupture simulations. In particular, the intermediate principal stress  $\sigma_2$  is assumed to be vertical ( $\sigma_1 > \sigma_2 > \sigma_3$ ). The Icelandic Stress Map from Ziegler et al. (2016) justifies this assumption. Based on the three best quality criteria from the world stress map project (Zoback et al., 1989; Zoback, 1992; Sperner et al., 2003; Heidbach et al., 2007, 2010), they choose  $SH_{max}$  (cf. Table 1) to set up a homogeneous regional stress field (Ziegler et al., 2016), which is consistent with previous estimates of the maximum horizontal stress from Angelier et al. (2004) and agrees with the local transtensional deformation pattern (Garcia and Dhont, 2004).

130 The stress shape ratio  $\nu = (\sigma_2 - \sigma_3)/(\sigma_1 - \sigma_2)$  facilitates the characterization of the stress regime and balances the principal stress amplitudes. Li et al. (2023) select  $\nu = 0.5$  corresponding to strike-slip faulting, which is supported by Ziegler et al. (2016) and the analysis of borehole breakouts, earthquake focal mechanism inversions, and geological data. It also agrees with assuming a  $90^\circ$  dipping fault system.

The dynamic rupture models use a linear slip-weakening (LSW) friction law with frictional cohesion to model frictional yielding and dynamic slip evolution (Ida, 1972; Andrews, 1976). The selected static and dynamic coefficients of friction ( $\mu_s$  and  $\mu_d$ ) are consistent with Byerlee’s law under the assumption that the increase of rock strength with depth is independent of rock type. The critical slip weakening distance  $D_c$  is lower within the nucleation zone for the models with the simpler fault geometry (Table 1).

140 The relative fault strength is expressed by the maximum pre-stress ratio  $R_0$ , the ratio of the potential stress drop to the breakdown strength drop (also known as strength excess).  $R_0 = (\tau_0 - \mu_d \sigma'_n)/((\mu_s - \mu_d) \sigma'_n)$ , where  $\tau_0$  represents the initial shear stress on the fault and  $\sigma'_n$  the initial effective normal stress. While in theory  $R_0 = 1$  implies critical prestress on a virtual optimally orientated plane (Biemiller et al., 2022),  $R_0$  falls between 0.9 and 0.55 in our models. In this study, we compare end-member dynamic rupture scenarios in terms of their generated vertical displacements and, thus, their potential to generate a tsunami. We also require that our comparison includes scenarios with comparable and plausible moment magnitude and dynamic stress drop. Our parameter choices fall within the range of uncertainty and sensitivities of the suite of dynamic rupture scenarios explored in Li et al. (2023). We chose a slightly higher  $R_0 = 0.9$  for all three dynamic rupture simulations on the complex fault geometry in comparison to their showcased complex fault geometry scenarios which use  $R_0 = 0.85$ . This results in a  $\sim 20\%$  average increase in vertical displacements compared to Li et al. (2023). To conserve comparable dynamic



stress drops with such increased  $R_0$ , we prescribe a slightly reduced pore fluid ratio  $\gamma = 0.7$  compared to their  $\gamma = 0.75$ . For the scenarios on the simpler fault geometry, we slightly increase  $\mu_s = 0.6$  (cf.  $\mu_s = 0.55$  in Li et al. (2023)) which again leads to slightly increased vertical uplifts but still matches local GMMs.

All rupture models are initiated smoothly in time and space by gradually reducing the fault strength ( $\mu_s$ ) at a predefined hypocentral location (Harris et al., 2018).

6 to 10 km is the inferred locking depth for the HFFZ (Metzger and Jónsson, 2014). The locking depth specifies the transition from seismic to aseismic faulting and limits the seismogenic part of a fault system (e.g., Rogers and Nason, 1971). Together with the consideration of the relocated seismicity from (Abril et al., 2018, 2019), the nucleation depth of all earthquake dynamic rupture scenarios is chosen to be at 7 km (Li et al., 2023).

Parameter	Models with simpler fault geometry	Models with complex fault geometry
Static friction coefficient ( $\mu_s$ )	0.6	0.55
Dynamic friction coefficient ( $\mu_d$ )	0.1	0.1
Critical slip distance ( $D_c$ ) within nucleation area [m]	0.2	0.4
Critical slip distance ( $D_c$ ) outside nucleation area [m]	0.5	0.4
$SHmax$	155	150*
Seismogenic depth [km]	10	10
Nucleation depth [km]	7	7
Maximum pre-stress ratio ( $R_0$ )	0.55	0.9
Pore fluid ratio ( $\gamma$ )	0.6	0.7
Stress shape ratio ( $\nu$ )	0.5	0.5
Nucleation patch radius ( $r_{crit}$ [km])	1.5	1.5

**Table 1.** Summary of dynamic rupture parameters chosen by Li et al. (2023) for the models with the simpler and complex fault geometry.

\*The orientation of the maximum horizontal stress is 150 for scenarios Complex-Middle and Complex-East but  $SHmax = 155$  for Complex-West.

### 2.3 Off-fault plastic yielding

All dynamic rupture models incorporate off-fault plasticity (Fig. A1). Accounting for off-fault deformation provides a more realistic representation of rupture dynamics in a fault zone with damaged host rock after the coseismic rupture phase (e.g., Antoine et al., 2022). We use a non-associative Drucker-Prager visco-plastic rheology (Wollherr et al., 2018) requiring assumptions on the bulk cohesion and the bulk friction as governing material parameters. Similarly to Li et al. (2023), the bulk friction is set according to the fault static coefficient of friction ( $\mu_s = 0.6$ ) which is constant in the elastic solid medium while bulk cohesion is depth-dependent and calculated as a function of the rigidity ( $C_{plast} = 0.0001\mu$ ).

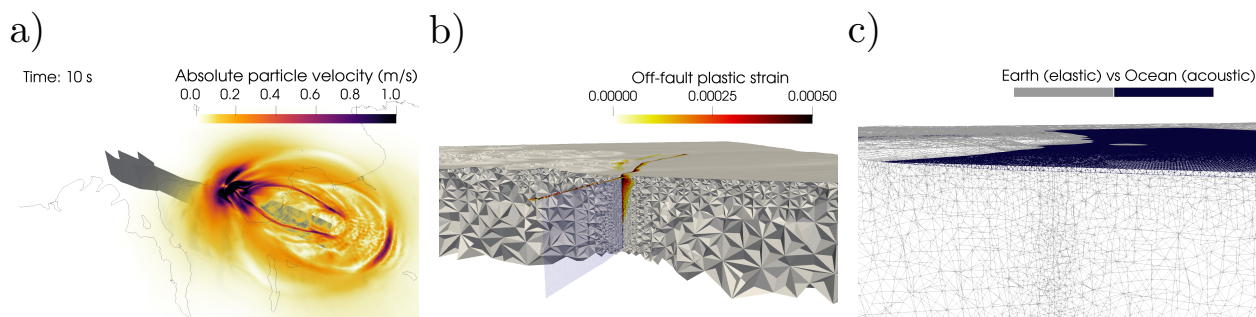


**Figure 3.** a) Snapshot at  $t = 10$  s of the simulated seismic wavefield for the earthquake dynamic rupture nucleating in the East of the simple fault geometry. b) Accumulated off-fault plastic strain ( $\eta$ ) at the end of simulation Simple-East forming a shallow flower structure. c) Mesh of the fully-coupled earthquake-tsunami simulation with the distinction between the elastic medium (Earth) and the acoustic medium (Ocean).

## 2.4 One-way linked methodology

165 We use the scientific open-source software package SeisSol (<https://github.com/SeisSol/SeisSol>, <http://www.seissol.org>) to numerically simulate six earthquake dynamic rupture scenarios on the HFFZ with three different epicenter locations (Fig. 2) on two fault system geometries (Sect. 2.1). SeisSol utilizes the arbitrary high-order accurate derivative discontinuous Galerkin method (ADER-DG) (Käser and Dumbser, 2006; Dumbser and Käser, 2006; de la Puente et al., 2009) and has been verified in community dynamic rupture benchmarks (Pelties et al., 2014; Harris et al., 2018). SeisSol achieves high-order accuracy in  
170 both space and time (Breuer et al., 2015; Uphoff et al., 2017; Krenz et al., 2021) and uses unstructured tetrahedral meshes to incorporate complex 3D bathymetry & topography and the complex fault geometries.

The one-way linked workflow uses the time-dependent seafloor displacement output from SeisSol to initialize sea surface perturbations within sam(oa)<sup>2</sup>-flash and has been successfully applied in Ulrich et al. (2019b), Madden et al. (2020), and Wirp et al. (2021). The dynamically adaptive, parallel software sam(oa)<sup>2</sup>-flash (<https://gitlab.lrz.de/samoa/samoa>) solves the non-  
175 linear hydrostatic shallow water equations (Meister et al., 2016). We apply the “Tanioka” filter (Tanioka and Satake, 1996), which takes the contribution of the horizontal ground deformation of the realistic bathymetry to the vertical displacement (Eq. B1) into account. However, the influence of the filter is negligible, likely due to the relatively flat seafloor surrounding the fault system without any large bathymetric gradients. The earthquake dynamic rupture scenarios are simulated for 100 s to ensure that seismic waves have reached the absorbing boundary conditions at the domain edges (Ramos et al., 2022). Each  
180 subsequent tsunami is simulated for 40 min which provides sufficient time for the tsunami to reach the coastline.





## 2.5 3D fully-coupled modeling

Traditional earthquake-tsunami modeling is often based on so-called two-step approaches (Abrahams et al., 2023) such as the one-way linked methodology introduced in Sect. 2.4. The fully-coupled method combines earthquake dynamic rupture and tsunami generation into one simulation aiming to capture the full physics of this process (Lotto and Dunham, 2015; Lotto et al., 2018; Wilson and Ma, 2021; Ma, 2022). 3D fully-coupled earthquake-tsunami modeling has recently been implemented in SeisSol, which allows us to account for the generation, propagation, and interaction of 3D elastic, acoustic, and tsunami waves, including dispersion effects, simultaneously (Krenz et al., 2021). The unstructured tetrahedral mesh is extended to include an additional water layer, which is necessary to include both an elastic medium (Earth) and an acoustic medium (Ocean) (Fig. 3). We incorporate the same resolution bathymetry in the fully-coupled model as used for the one-way linked workflow. The geometric union of fault geometry, subsurface, and the ocean is non-trivial. The higher computational cost associated with adding oceanic acoustic and tsunami wave simulation requires a reduction of the modeling domain, which we achieve by prescribing a water layer that is laterally smaller than the Earth modeling domain (Fig. 3). Within the water layer, we set the rigidity equal to zero ( $\mu = 0$ ). This ensures the suppression of S-waves in the liquid medium, and we obtain an acoustic wave speed of  $\sim 1500 \text{ m s}^{-1}$ . The simulated time is 3 min, which allows us to compare the initial tsunami generation and capture the complex superposition of seismic, acoustic, and tsunami waves. Our fully-coupled simulation time is chosen accordingly to avoid waves reaching beyond the edges of the water layer model extent. The spatial discretization within the water layer is 200 m. We use a polynomial order of  $p = 4$  (i.e., fifth-order of accuracy in time and space). 200 m is here the used on-fault resolution which is gradually coarsened away from the HFFZ to a maximum size of 5 km at the edges of the elastic medium.

Based on the six scenarios using the one-way linked approach, we analyze the three plausible “worst-case” tsunamigenic scenarios on the simpler fault geometry with the fully-coupled approach, Simple-West, Simple-Middle, and Simple-East. All dynamic rupture initial conditions are kept the same as they were in the respective linked scenarios.

## 3 Results

### 3.1 Dynamic Rupture

The earthquake dynamic rupture scenarios with nucleation in the West and East of the complex fault geometry yield a significantly smaller moment magnitude than the other four scenarios, which is reflected in the moment rates (Fig. 4). Their rupture fronts propagate only  $\sim 30$  km due to the high fault segmentation and fault gaps inhibiting dynamic triggering and multiple rupture jumps. While the scenario on the complex fault geometry with the hypocenter in the middle breaks a greater extent of the fault system, its seismic moment is still smaller than all three scenarios on the simpler fault geometry due to reduced maximum fault slip and the smaller ruptured area. A comparison of the fault slip distributions can be seen in Fig. A2. All earthquake dynamic ruptures on the simpler fault geometry break over the entire main fault length and generate larger maximum slip. Scenario Simple-East produces the largest maximum fault slip at the offshore section of the fault system (7.90 m, Table 2).



Furthermore, the three earthquake dynamic rupture simulations on the simple fault geometry cause significant shallow fault slip resulting in a negligible shallow slip deficit (SSD) (Fig. A3). The SSD is defined as the potential reduction of near-surface slip in comparison to slip at seismogenic depths (e.g., Fialko et al., 2005; Marchandon et al., 2021). Our six dynamic rupture simulations show the accumulation of plastic strain surrounding the fault traces (Fig. A1), where the resulting off-fault plastic strain distribution with depth (Fig. 3) resembles a shallow flower-shape structure enclosing the fault (e.g., Ben-Zion et al., 2003; Rockwell and Ben-Zion, 2007; Ma, 2008; Ma and Andrews, 2010; Schliwa and Gabriel, 2022).

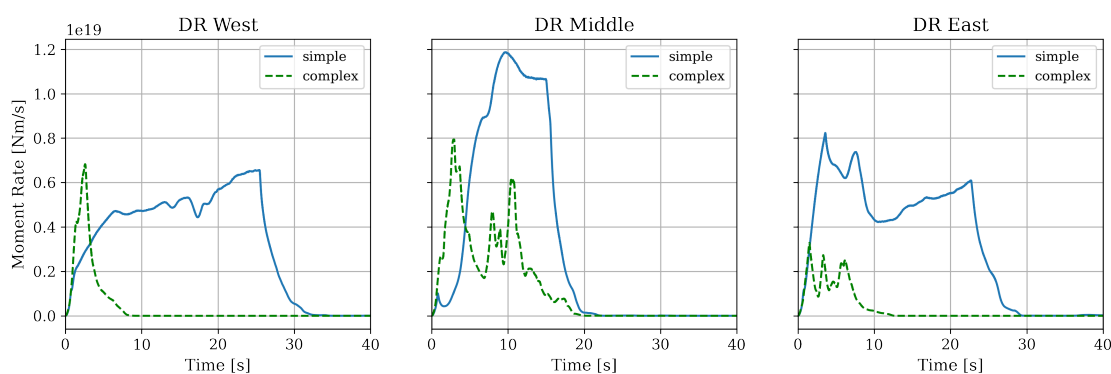


**Figure 4.** Moment release rates for the six earthquake dynamic rupture (DR) simulations (up to  $t = 40$  s). Multiple peaks for Complex-Middle and Complex-East correspond to the rupture decelerating before jumping to (that is, dynamically triggering) the next fault segment.

### 3.1.1 Seafloor Displacement

The coseismic earthquake displacements we observe are non-negligible and reach up to  $\sim 1$  m of seafloor uplift and up to  $\sim 0.8$  m of subsidence (Table 2) for ruptures on the simpler fault with nucleation in the East and Middle of the HFFZ. The earthquake dynamic rupture simulation with the western hypocenter on the simpler fault geometry reveals that major displacement occurs onshore (Fig. 5). This has a significant impact on seismic hazard assessment, in particular for the town of Húsavík, which is located directly above the HFFZ. However, the tsunami potential of scenarios with Western epicenters is expected to be smaller.

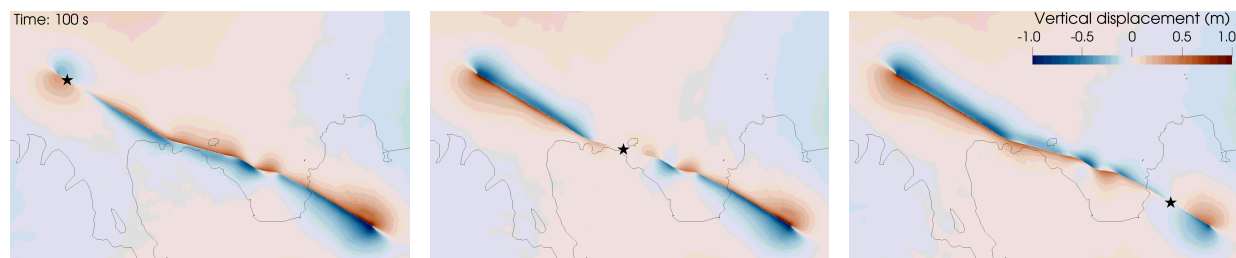
While the maximal coseismic seafloor subsidence of the simulation Complex-Middle is equivalent in size to the maximum subsidence observed for the scenarios on the simpler fault geometry, the rupture generates only half as much uplift (Table 2). The total offset of the vertical displacement for the scenario Complex-Middle is  $\sim 1.2$  m), which matches the vertical offset for scenario Complex-West. However, the latter offset is restricted to the western end of the HFFZ north of Siglufjörður and Eyjafjörður Bay. Meanwhile, the displacement pattern of scenario Complex-East mainly affects Skjálfandi Bay and Húsavík.

### 3.1.2 Rake

The rake of an earthquake is defined as the angle between the strike and slip directions and describes how the adjacent blocks of the fault plane move during rupture (Aki and Richards, 2002). We expect a rake of  $180^\circ$  for a vertically dipping right-



a)



b)

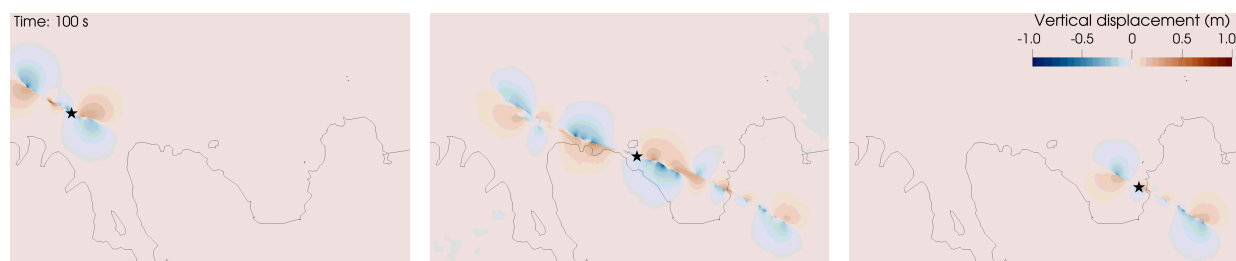


**Figure 5.** Uplift and subsidence from the surface displacements of earthquake dynamic rupture simulations after accounting for local bathymetry using the Tanioka filter (Tanioka and Satake, 1996) on a) the simple fault geometry and b) the complex fault geometry. Black stars mark the epicenter locations.

lateral strike-slip fault system. However, we observe dynamic rake rotation ( $\pm 20^\circ$ ) near the surface during the rupture (Fig. 6). In our models, dynamic rake rotation (interacting with local bathymetry) explains the higher-than-expected vertical seafloor displacements due to the transient changes in slip direction inducing dip-slip components.

### 3.2 Time-dependent tsunami generation

The coastline of North Iceland includes several smaller islands, like Flatey Island, Grímsey Island, and Hrísey Island. Furthermore, the region of Norðurland eystra in North Iceland includes steep terrain, elongated fjords such as Eyjafjörður and bays with a shallower shoreline like Skjálfandi Bay. Accounting for these diverse coastal features and complex 3D bathymetry off-shore Northern Iceland, we analyze the one-way linked scenarios with simulation times long enough to compare the tsunami's impact at synthetic tide gauge stations placed near coastal towns in Sect. 3.2.1. In Sect. 3.2.2, we use fully-coupled scenarios on the simpler fault geometry to study the full dynamics of tsunami generation and earthquake-tsunami interaction.

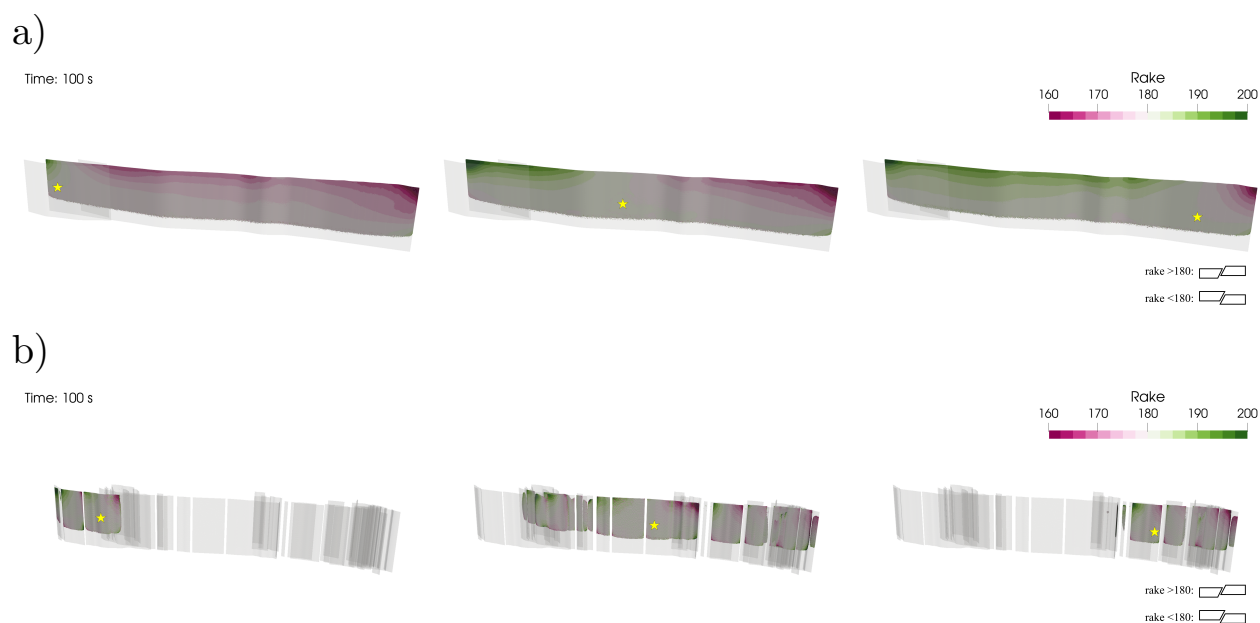


**Figure 6.** Dynamic rake rotation in the dynamic rupture simulations on a) the simple fault geometry and b) the complex fault geometry. Yellow stars mark the hypocenter locations. A rake of 180 degrees indicates pure right-lateral strike-slip faulting.

	simple fault geometry			complex fault geometry		
	West	Middle	East	West	Middle	East
Hypocenter						
$M_W$	7.34	7.33	7.34	6.74	7.07	6.68
Max. fault slip [m]	10.34	8.11	7.90	3.50	5.23	2.74
Max. fault slip offshore [m]	6.93	6.58	7.90	3.50	5.23	2.74
Max. peak slip rate [ $\text{m s}^{-1}$ ]	15.05	14.93	15.14	10.44	11.59	8.66
Max. peak slip rate offshore [ $\text{m s}^{-1}$ ]	13.53	12.58	15.14	10.44	11.59	8.62
Max. seafloor uplift [m] (after Tanioka filter)	0.75	1.05	0.95	0.56	0.44	0.23
Max. seafloor subsidence [m] (after Tanioka filter)	-0.74	-0.79	-0.76	-0.66	-0.79	-0.42

**Table 2.** Key results of our here considered six earthquake dynamic rupture scenarios. Note that we only show the maximum offshore coseismic vertical displacements (i.e., seafloor offsets) in the table because the onshore vertical displacements do not contribute to the tsunami generation.

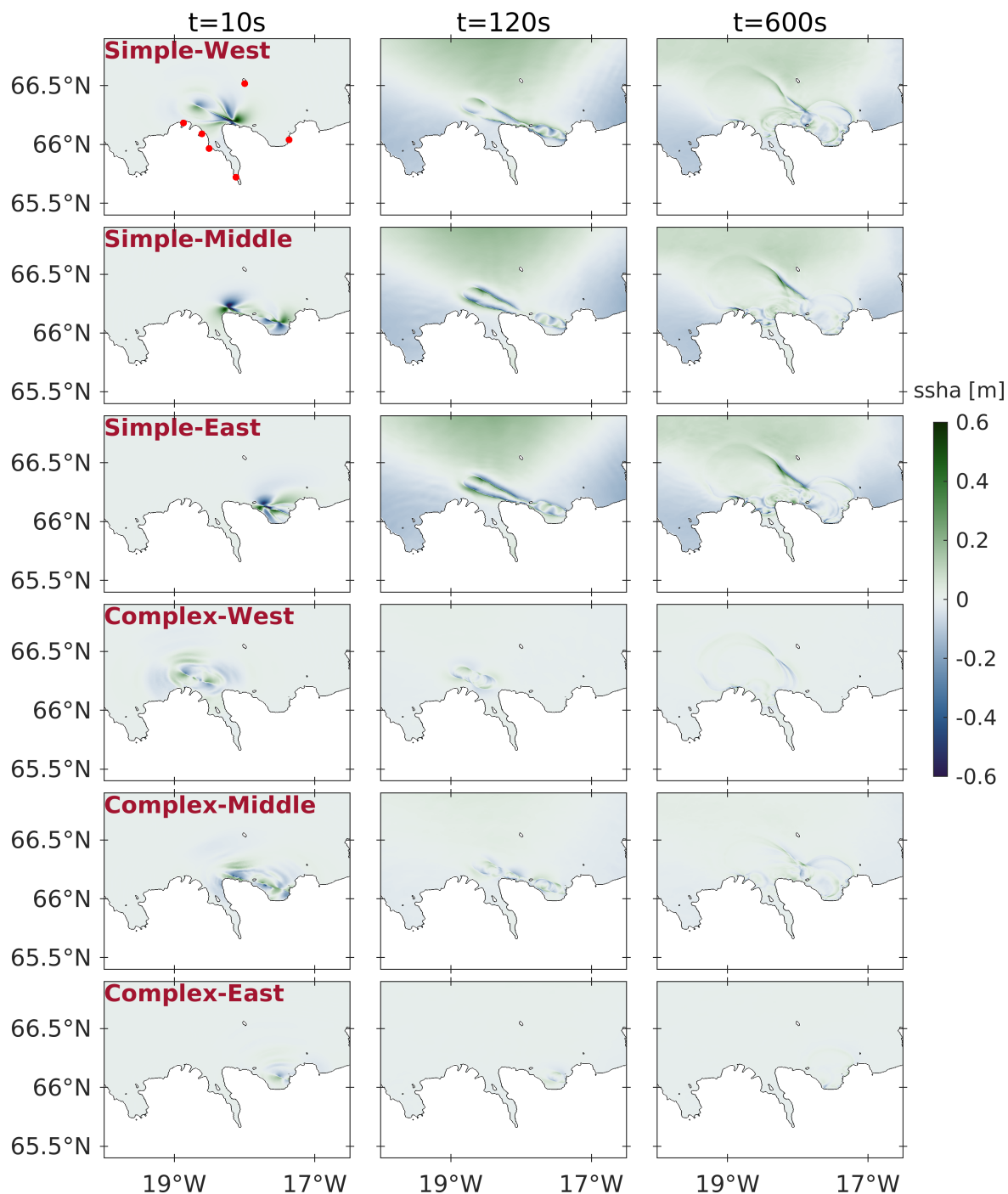


**Figure 7.** Sea surface height anomaly (ssha) of all six one-way linked earthquake-tsunami scenarios at 10 s (first column), 2 min (second column), and 10 min (third column) simulation times. The red points in the top-left panel mark the position of synthetic tide gauges near the coastal towns Siglufjörður, Ólafsfjörður, Dalvík, Akureyri, Húsavík (west to east on the mainland) and Grímsey Island.



### 3.2.1 One-way linked scenarios

We define the sea surface height anomaly (ssha) as deviation from the ocean surface at rest. We place six synthetic tide gauge stations offshore, in direct proximity to the towns of Húsavík, Akureyri, Dalvík, Ólafsfjörður, Siglufjörður and Grímsey Island. Every tsunami is simulated for 40 min.

We show snapshots of tsunami propagation after 120 s and 600 s in Fig. 7. The first column in Fig. 7 shows the complexity of the time-dependent seafloor displacements in all dynamic rupture sources superimposing seismic wave propagation after 10 s.

We first analyze the three one-way-linked tsunami scenarios sourced by dynamic rupture simulations on the simpler fault geometry which cause overall larger wave heights. All dynamic ruptures on the simpler fault geometry are still propagating after 10 s. The corresponding snapshots in Fig. 7 highlight source directivity effects for the simple-fault-geometry scenarios. Earthquake ruptures in the scenarios Simple-Middle and Simple-East arrive at Skjálfandi Bay within the first seconds. The unilateral dynamic rupture in scenario Simple-West requires more time to propagate eastwards towards Húsavík and causes a higher maximum ssha of 27 cm at the corresponding synthetic tide gauge (Fig. 8 and 9).

The initiating tsunami wavefronts from scenarios Simple-East and Simple-Middle evolve similarly, visible in the snapshots at 2 min and 10 min propagation time. In distinction, while the tsunami front from scenario Simple-West appears at a comparable location, its sea surface height anomaly is smaller than the ssha from the previous two scenarios. The synthetic tide gauge stations reveal that scenario Simple-East produces slightly larger wave amplitudes than the other two scenarios on the simpler fault geometry (with an exception at station Húsavík, cf. Fig. 8 and 9). Scenario Simple-East generates a maximum crest-to-valley difference (wave height) of 0.9 m near Ólafsfjörður. Positive amplitudes (i.e., the maximum distance between the highest point of a tsunami wave crest and the ocean at rest) greater than 30 cm can also be observed near Dalvík and Grímsey Island. The Scenario Simple-East tsunami continues propagating towards Akureyri but with locally significantly decreased amplitudes.

Overall, the tsunami scenarios initiated by dynamic rupture scenarios on the complex fault geometry cause smaller tsunamis (Fig. 7, see bottom three rows). In contrast to the scenarios on the simpler fault geometry, now the respective tsunami characteristics are highly dependent on epicentral location. The tsunami in scenario Complex-West arrives at the tip of Iceland's north coast within the first 5 min and then propagates directly into the bay of Eyjafjörður, arriving at Dalvík at around 10 min (Fig. B1). Wave heights for scenario Complex-West exceed ~20 cm at Siglufjörður and Grímsey Island and are the largest among the three scenarios on the complex fault geometry in Ólafsfjörður with ~40 cm.

The tsunami scenario caused by dynamic rupture in the middle of the complex Húsavík-Flatey Fault, in scenario Complex-Middle, affects the town of Húsavík within the first minute. Wave heights reach ~20 cm at several locations across Skjálfandi Bay. The tsunami enters the neighboring fjord Eyjafjörður arriving in Dalvík after approximately 15 min, with amplitudes up to ~10 cm, but again decays before reaching Akureyri. The tsunami generated in scenario Complex-East remains completely bounded by the bay surrounding Húsavík. Consequently, waves only expand within Skjálfandi Bay for about 10 min reaching

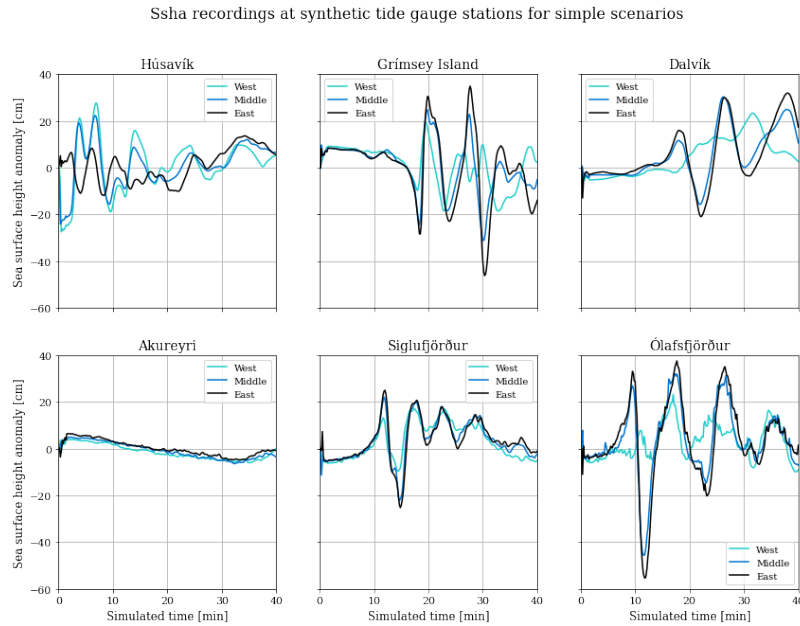


**Figure 8.** Sea surface height anomaly (ssha [cm]) vs simulation time (40 min) for three one-way-linked scenarios sourced by dynamic rupture simulations on the simpler fault geometry recorded at six synthetic tide gauge stations close to the towns Húsavík, Akureyri, Dalvík, Ólafsfjörður, Siglufjörður and Grimsey Island.

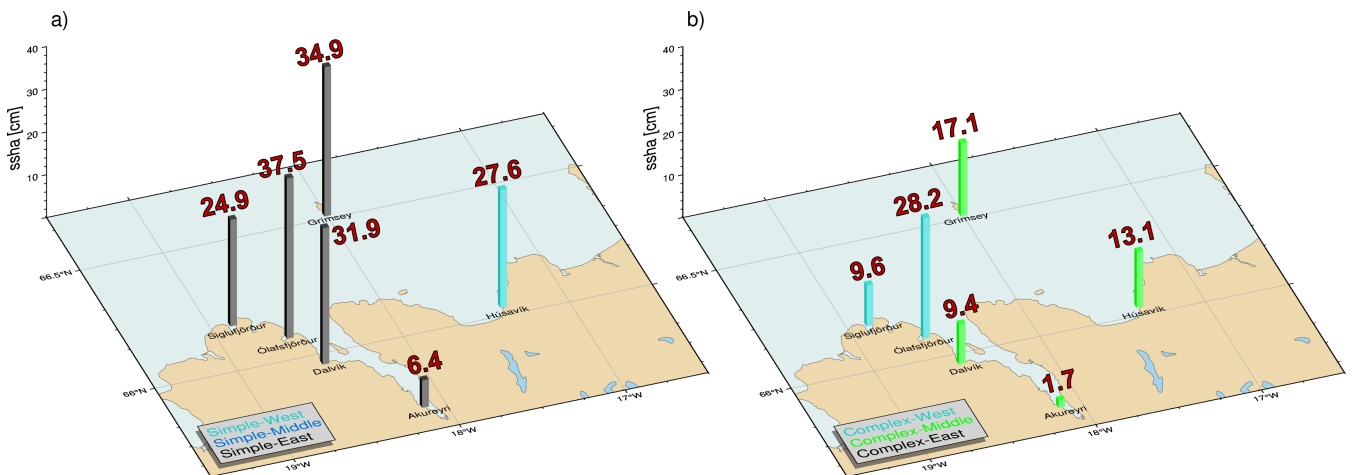


**Figure 9.** Maximum sea surface height anomaly (ssha [cm]) recorded throughout the simulation time of 40 minutes at synthetic tide gauge stations nearby local communities in North Iceland for the one-way linked scenarios based on the simpler fault geometry (a) and the complex fault geometry (b). At each tide gauge, we show the maximum ssha of all three respective scenarios, with bar colors indicating the epicentral location of the scenario causing maximum ssha at a given location.



ssha on the order of  $\pm 10$  cm. Due to its lower wave heights, this tsunami marginally signals at any of the other synthetic tide gauge stations.

### 3.2.2 3D fully-coupled scenarios

Based on the results from the one-way linked simulations we select those earthquake-tsunami scenarios causing larger wave heights for the computationally more demanding fully-coupled models. A single fully-coupled simulation of joint dynamic rupture and tsunami generation (for 3 min of simulated time) requires  $\sim 4$  h computational time with 40 nodes (1920 cores) on SuperMUC-NG, that is, a total of 7680 CPUh. To first order, the fully-coupled tsunami simulations match the seismic and tsunami waveforms obtained using the one-way linked approach (Fig. B2). Seismic waves result in transient motions of the sea surface and affect the ocean response but do not appear to contribute to tsunami generation. However, in the fully-coupled simulations seismic waves within Earth, acoustic waves within the ocean, and wave conversions superimpose. We show the three 3D fully-coupled dynamic rupture scenarios using the simple fault geometry in Figs. 10, 11, 12 to better understand the dynamic tsunami generation and complex superposition of different wave types. Their interaction is visible in panels (a) and (c), where we illustrate the sea surface height anomaly (ssha) and sea surface vertical velocity (ssvv) after 20 s simulated time. Close to the fault, we see the excited tsunami waves, best visible in panels (a), which start to propagate away from the ruptured fault system. At the same time, faster propagating acoustic waves already approach the water layer boundaries. We select two profiles approximately perpendicular to the fault system's strike direction of each fully-coupled scenario, with their bathymetry shown in panels (b). Along these two cross-sections, we plot the space-time evolution of ssvv in the respective panels (d) of Figs. 10, 11, 12. They indicate distinct features.

First, the propagation of the tsunami at a speed of  $\sim 35$  m s<sup>-1</sup> towards the open ocean. The tsunami waves in all three scenarios travel 5.6 km in 160 s (cross-section 2 Figs. B3, B4, B5). A slightly larger – yet comparable – value of  $\sim 41.8$  m s<sup>-1</sup> can be calculated using the relation  $\sqrt{g \cdot H}$  for the tsunami velocity, approximating the gravitational acceleration as  $g = 10$  m s<sup>-2</sup> and the average water depth as  $H = 175$  m from cross-section 2 in panel (b) of Figs. 10, 11, 12. The tsunami waves visible in cross-section 1 of all panels (d) show a decrease in wave velocity (now  $\sim 20$  m s<sup>-1</sup>) as the tsunami front approaches the shoreline, which is located at 0 km. This expected effect is caused by the reduction of the local bathymetry to less than 40 m depth, evident at a distance of 20 km away from the coast (Figs. 10, 11, 12, (b), cross-section 1).

Second, we observe the complex seismo-acoustic wave excitation and interaction in the initial phase of tsunami generation. The high-amplitude acoustic waves are clearly visible in all three scenarios. The seismic-generated acoustic waves propagate at a speed of  $c_0 = 1500$  m s<sup>-1</sup> and are, therefore, much faster than the oceanic tsunami. Importantly, the ssvv amplitudes caused by the acoustic waves are larger than those corresponding to the actual tsunami.

Next to ocean acoustic waves, we observe normal dispersion, i.e. frequency-dependent wave speeds, of the tsunami (Fig. 13). We use the same two cross-sections as before and show ssha (rows one and three, Fig. 13) and ssvv (rows two and four, Fig. 13) at a simulated time of 2 min for the three scenarios on the simpler fault geometry, given both tsunami modeling techniques. The one-way linked tsunami waveforms (dashed black line) for both cross-sections in the first and third row are rather smooth. Their overall trend including the spatial location of peaks and troughs is well matched by the corresponding fully-coupled





310 waveforms (solid blue line). However, a close look into the waveforms indicates additional short-period signals in-between wave crests and troughs. A zoom into the sea surface vertical velocities, shown in rows two and four of Fig. 13, reveals multiple distinct wavefronts reflecting normal dispersion effects. In contrast, anomalous dispersion, where shorter wavelengths (higher frequencies) propagate faster than longer wavelengths (lower frequencies), can not be identified in our simulations, which is expected due to the locally shallow ocean (Abrahams et al., 2023).

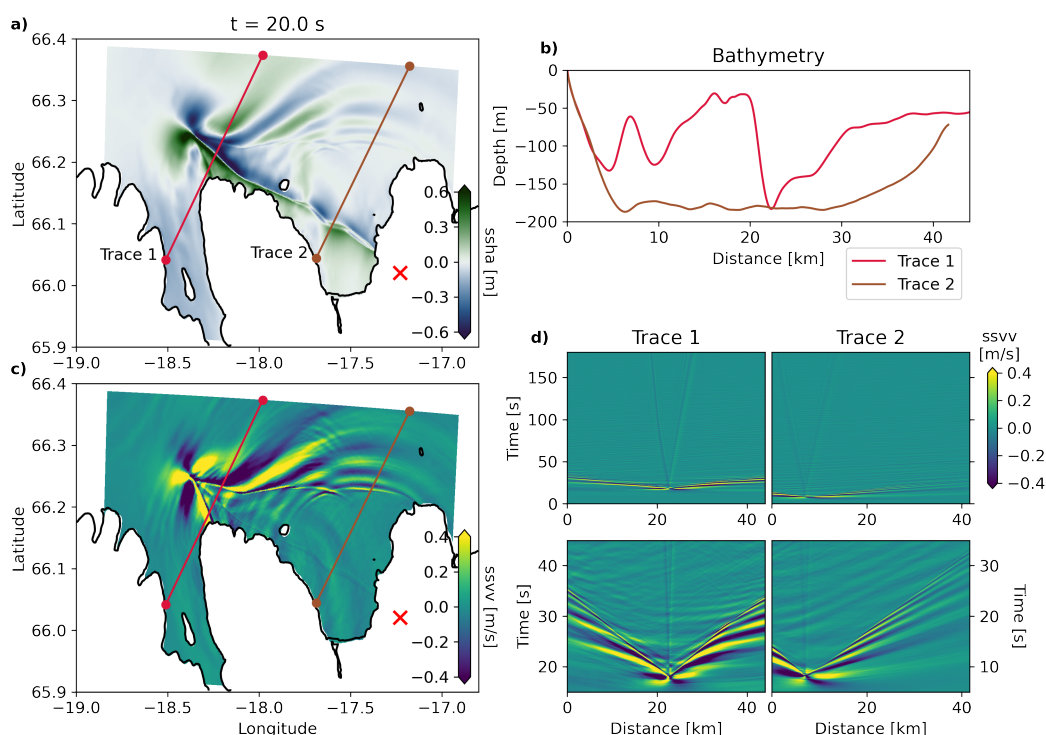


**Figure 10.** 3D fully-coupled earthquake-tsunami scenario Simple-East, with dynamic rupture on the simple fault geometry and a hypocenter in the East (red cross). Snapshots at  $t = 20$  s of a) the sea surface height anomalies (ssha) and c) sea surface vertical velocity (ssvv). b) Corresponding bathymetry profiles along the two selected cross-sections stretching from the shoreline (0 km) towards the open ocean. d) Space-time evolution of ssvv along the two cross-sections for the full duration of the fully-coupled simulations (upper row, highlighting the tsunami) and the superposition of near-field displacements, seismic and acoustic waves, and tsunami generation (lower row, highlighting the fast propagating acoustic waves). A larger version of panel d), where we annotate the acoustic and tsunami waves, is shown in Fig. B3.

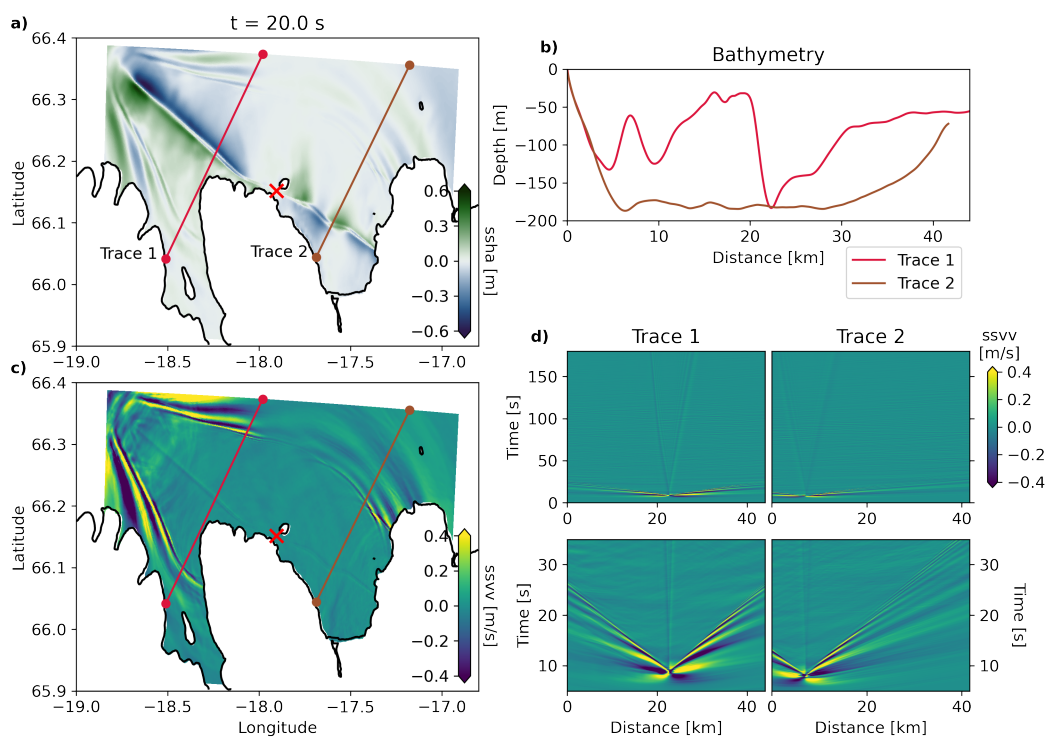


**Figure 11.** Same as Fig. 10 but for scenario Simple-Middle (red cross marks the epicenter). A larger version of panel d), where we annotate the acoustic and tsunami waves, is shown in Fig. B4.

#### 315 4 Discussion

Submerged ruptures across strike-slip fault systems were long assumed to produce only minor vertical offsets and hence no significant disturbance of the water column. During the 2018  $M_W$  7.5 Sulawesi earthquake in Indonesia, linked and fully-coupled earthquake dynamic rupture and tsunami modeling imply that coseismic-induced seafloor displacements were a critical component generating an unexpected and devastating local tsunami in Palu Bay (Ulrich et al., 2019b; Krenz et al., 2021; 320 Ma, 2022). In this study, we use six earthquake dynamic rupture simulations with varying hypocenter locations and fault system complexity to show that the Húsavík-Flatey Fault Zone can host tsunamigenic earthquakes. This may have important implications for tsunami hazard assessment of submarine strike-slip fault systems in transform and transtensional tectonic settings worldwide. For example, the North-Alfeo Fault in the Ionian Sea may be capable to generate a  $M_W \approx 7$  strike-slip earthquake (Scicchitano et al., 2022), but is often not considered in tsunami modeling.

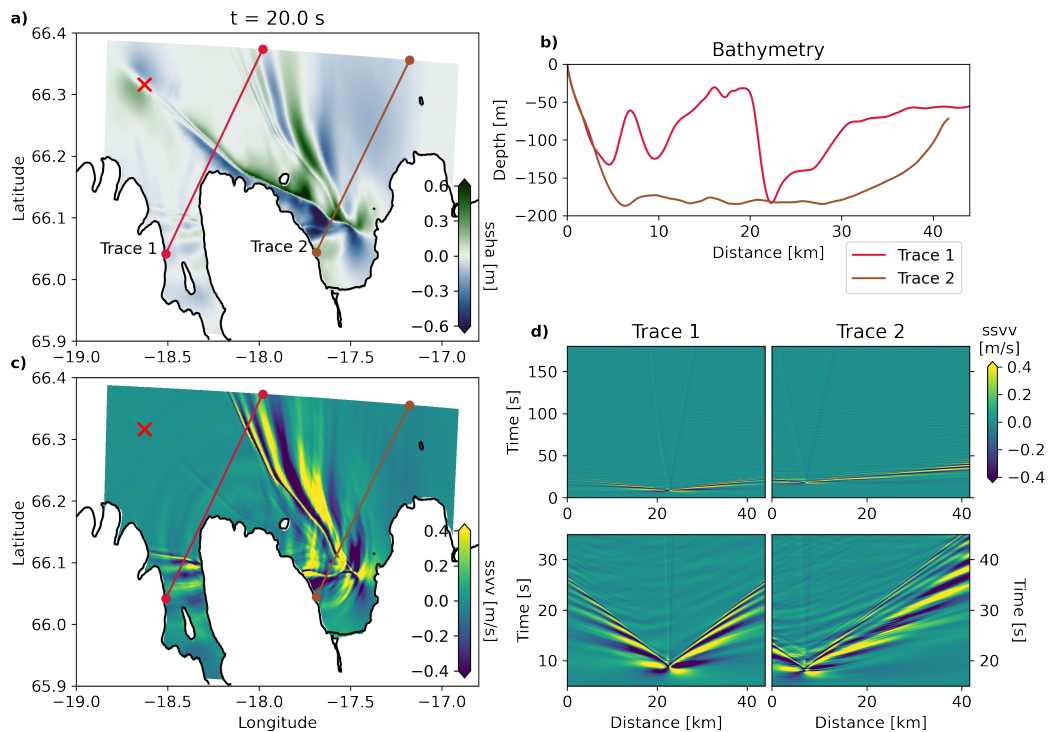


**Figure 12.** Same as Fig. 10 but for scenario Simple-West (red cross marks the epicenter). A larger version of panel d), where we annotate the acoustic and tsunami waves, is shown in Fig. B5.

325 Our earthquake dynamic rupture scenarios can generate enough vertical seafloor displacements to source a localized tsunami. The scenarios on the simpler fault geometry may be considered worst-case events because the ruptures break over the entire main fault length accumulating large fault slip (equivalent to  $\sim M_W 7.3$ ). The moment magnitudes of our dynamic rupture models on the complex fault geometry are lower ( $M_W 6.7 - M_W 7.0$ ) and involve more segmented slip due to rupture-jumping across the highly segmented fault network. For all scenarios, we observe pronounced dynamic rake rotation near the surface.

330 The dynamic deviations from pure right-lateral strike-slip faulting are on the order of  $\pm 20^\circ$  and introduce dip-slip motion. Rake rotation has been inferred for surface-breaking earthquakes using geological slickenlines (Kearse et al., 2019; Kearse and Kaneko, 2020) and enhances vertical displacements in our simulations, which are critical for tsunami generation. In difference to a proposed dominance of off-fault deformation in strike-slip tsunami generation in Palu Bay (Ma, 2022), the effect of off-fault plasticity is likely small in our simulations. We find that off-fault deformation contributes only about  $\sim 3\%$  of the total

335 seismic moment.

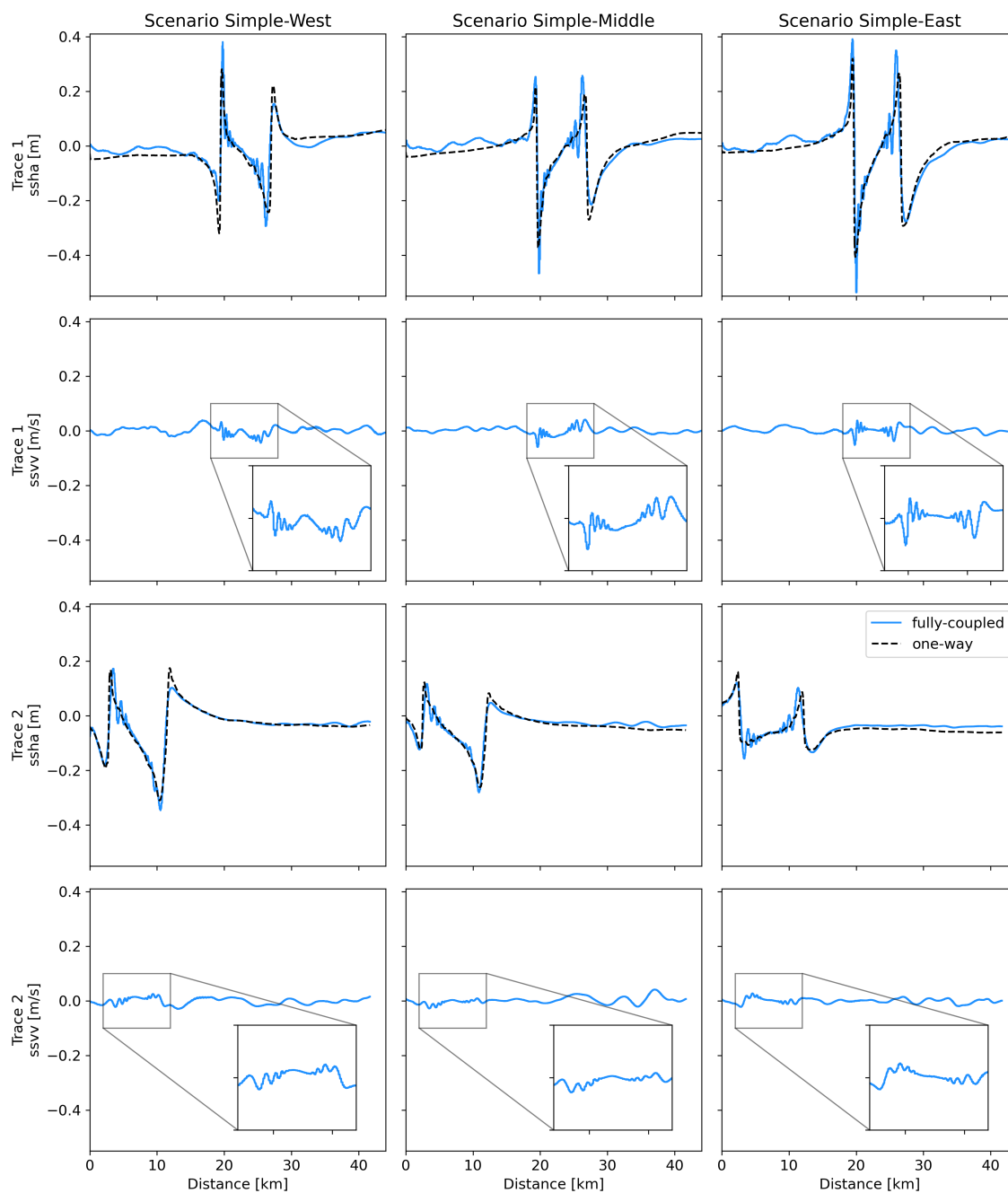


**Figure 13.** Sea surface height anomaly (ssha) along previous two cross-sections at  $t=2$  min for the fully-coupled (solid blue line) and one-way linked (dashed black line) scenarios on the simpler fault geometry in the first and third row. Sea surface vertical velocity (ssvv) for all fully-coupled simulations highlighting tsunami normal dispersion in the second and bottom rows. The shoreline is located at 0 km.



Modeling tsunami scenarios for hazard assessment or rapidly after submarine earthquakes often relies on simplifications, such as the negligence of source time-dependency, only considering vertical seafloor deformation without bathymetry effects, solely planar fault geometries, or neglecting tsunami dispersion and acoustic wave effects. Abrahams et al. (2023) introduce non-dimensional parameters allowing quantifying the range of validity for certain modeling assumptions. Our average water  
340 depth  $H$  can be approximated as  $\sim 200$  m, the source width  $\sigma_r$  as given by the length of the HFFZ ( $\sim 100$  km), the source duration  $\sigma_t$  of 30 s constrained by the rupture duration (cf. moment rates Fig. 4), the gravitational acceleration  $g = 10 \text{ m s}^{-2}$  and acoustic wave speed  $c_0 = 1500 \text{ m s}^{-1}$  we can calculate the three non-dimensional numbers posed by Abrahams et al. (2023) as specified in Table 3.

We see that the shallow water limit is fulfilled ( $H/\sigma_r \ll 1$ ), which justifies using our one-way linked earthquake-tsunami  
345 modeling approach. While we use time-dependent seafloor displacements, our source should appear effectively as instantaneous to tsunami waves ( $\sqrt{gH} \cdot \sigma_t/\sigma_r \ll 1$ ) due to the relatively short rupture duration and shallow water depth. This fact explains the similarity in the tsunami propagation and shape of the tsunami wavefronts for the simple fault geometry scenarios, which all break the entire main fault length and lead to similar fault slip distributions. In contrast, the scenarios on the complex fault geometry differ distinctly in their final fault slip distributions and areas of seafloor displacements depending on the chosen  
350 epicenter location. However, to compare the tsunami generation phase, it is indispensable to consider a time-dependent source model for both approaches, the one-way linked and fully-coupled method, for comparability.

From the average water depth  $H$  being much smaller than  $c_0 \cdot \sigma_t$  (Table 3) we expect that it is justified to neglect acoustic wave excitation since their amplitudes should be small. However, our fully-coupled simulations include acoustic wave generation with high amplitudes, larger than tsunami signals, (Figs. 10, 11, 12). Dynamic rupture reaching the Earth's surface can cause  
355 strong radiation (Kaneko and Goto, 2022) including the generation of high-frequency seismic waves due to the locally strong deceleration at the rupture front (e.g., Madariaga et al., 2006; Okuwaki et al., 2014; Li et al., 2022). Part of this seismic wave energy is converted to ocean-acoustic waves at the seafloor (e.g., Krenz et al., 2023), as observed during the 2011 Tohoku-Oki (e.g., Maeda et al., 2013) and the 2003 Tokachi-Oki earthquakes (e.g., Nosov and Kolesov, 2007) using ocean-bottom pressure sensors. Earlier studies found that the conversion between seismic and ocean acoustic waves occurs predominantly at slopes of  
360 the seafloor (e.g., Noguchi et al., 2013). Here, however, local bathymetry is generally flat, and the conversion is dominated by dynamic source complexity, such as surface rupture and the associated shallow rake rotation.

In our study, we compare a simple fault geometry representing the Húsavík-Flatey Fault Zone and a very complex fault network consisting of 55 individual fault segments. Klinger (2010) and Lefevre et al. (2020) proposed a linear relationship between the thickness of the seismogenic crust (brittle upper crust) and the length of fault segments for strike-slip geometries.  
365 This would imply a relatively short average fault segment length given the locking depth of 6 – 10 km for the HFFZ (Metzger and Jónsson, 2014). Therefore, during a large strike-slip earthquake along the HFFZ, rupture may segment into several subevents (Jiao et al., 2021; Klinger, 2022), as resembled in our Complex-Middle scenario. However, Iceland, offering a unique geologic complexity, is located atop the Mid-Atlantic Ridge and influenced by the underlying mantle plume (Torsvik et al., 2015; Celli et al., 2021) with significantly varying crustal thickness over the last 56 Ma (Hjartarson et al., 2017), potentially



370 altering established scaling relation. Hence, it is important to include different fault structural complexity within earthquake and tsunami simulations to accurately capture plausible earthquake scenarios.

The three tsunami scenarios sourced by dynamic rupture simulations across the complex fault geometry cause significantly smaller tsunamis. This is due to lower and more segmented fault slip leading to less vertical seafloor displacements, which are spatially more restricted. The largest total wave height (i.e., crest-to-trough difference) of  $\sim 40$  cm is observed at the synthetic  
375 tide gauge stations near Grímsey Island for scenario Complex-Middle and near Ólafsfjörður for Complex-West. The tsunami from scenario Complex-East does not have a significant impact on the virtual tide gauges since much of the coseismic ground displacement occurs onshore. The town Ólafsfjörður is also highly exposed to tsunami signals in the scenarios using the simpler fault geometry with wave heights reaching 0.9 m.

We find that our scenario Simple-East poses the largest impact for coastal communities, except for Húsavík. Here the  
380 hypocenter is near the town, which may experience strong ground shaking (Li et al., 2023), but not a large tsunami. However, Húsavík can be affected by scenario Simple-West causing nearly 60 cm crest-to-trough difference. This unilateral rupture nucleating at the western end of the HFFZ builds up energy while propagating towards Húsavík, explaining the larger observations. We find that none of our scenarios endanger the town of Akureyri, which is shielded by the narrow Eyjafjörður. The modeled tsunami does not amplify but loses energy due to multiple reflections within the bay and due to the protection by  
385 Hrísey Island.

Ruiz-Angulo et al. (2019) performed a preliminary investigation of the tsunami potential for the Húsavík-Flatey Fault Zone using a uniform fault-slip earthquake dislocation source with a moment magnitude of 7.0, located in the middle of the fault system. They utilized the Okada method (Okada, 1985) with instantaneous sourcing of the tsunami by the final static displacements. Their maximum synthetic crest-to-trough difference of  $\sim 30$  cm also occurs at Ólafsfjörður. While this is slightly larger  
390 than the maximum crest-to-trough difference of 26 cm which we observe for the scenario Complex-Middle, it is a factor of 2.5 smaller than our scenario Simple-Middle (77 cm).

These differences may be due to our dynamic rupture models including dynamically evolving relatively large shallow fault slip (up to  $\sim 8$  m for Simple-East) with no SSD for scenarios on the simpler fault geometry and near-surface rake rotation ( $\pm 20^\circ$ ). This results in higher-than-expected coseismic vertical displacements ( $\pm 1$  m). In addition, we include local bathymetry  
395 and, to a smaller extent, off-fault plastic deformation, all contributing to the tsunami generation.

Ruiz-Angulo et al. (2019) also report on earthquake-landslide-linked tsunami scenarios, which are plausible and need to be investigated further, but are beyond the scope of this work's modeling techniques. Our six one-way linked scenarios show that the fault geometry can influence the subsequent tsunami generation. Future studies may explore potential variations in fault dip, which may further enhance the vertical seafloor displacement during the earthquake rupture. Similarly, accounting for the  
400 potential existence of shallow, weak sediments, which are more prone to off-fault plastic deformation, may increase local uplift (Seno and Hirata, 2007; Ma and Nie, 2019; Wilson and Ma, 2021; Ulrich et al., 2022).

Our 3D fully-coupled simulations include unexpectedly high-amplitude acoustic waves, which may serve as a rapid indicator of surface dynamic rupture. Such acoustic wave signals may be used to improve tsunami early warning since these can be detected earlier, e.g., at ocean bottom pressure sensors, in comparison to the tsunami recorded at conventional DART buoys



405 (Yamamoto, 1982; Cecioni et al., 2014; Mei and Kadri, 2017; Gomez and Kadri, 2021). Next to the seismo-acoustic wave  
excitation, we observe dispersion of tsunami propagation velocity (Tsai et al., 2013). Glimsdal et al. (2013) showed that  
dispersion effects may be expected for moderate-magnitude earthquakes. Accounting for dispersion effects can be important if  
the resulting series of excited oceanic waves locally interfere constructively and amplify, which has been observed in tsunami  
scenarios of the South China Sea (Ren et al., 2015) and outer-rise normal faults (Baba et al., 2021). Here, we do not detect  
410 significant differences in wave height or tsunami arrival times compared to our one-way linked scenarios, despite dispersion  
effects. Likely reasons include the on-average shallow water depth and the close proximity of the HFFZ to the coast preventing  
interferences.

Source width $\sigma_r$ (m)	Source duration $\sigma_t$ (s)	Instantaneous source $\sqrt{gH} \cdot \sigma_t / \sigma_r \ll 1$	Negligible acoustic wave excitation $H / (c_0 \cdot \sigma_t) \ll 1$	Shallow water limit $H / \sigma_r \ll 1$
100.000	30	Justified	Justified	Justified

**Table 3.** Non-dimensional parameters for the justification of modeling assumptions as introduced by Abrahams et al. (2023). The parameter  $H$  is the average water depth ( $\sim 200$  m),  $c_0$  is the acoustic wave speed of  $1500 \text{ m s}^{-1}$ , and  $g$  is the gravitational acceleration.

## 5 Conclusions

We present a suite of realistic earthquake-tsunami scenarios for North Iceland comparing one-way linked and 3D fully-coupled  
415 modeling techniques. Both approaches agree in the resulting sizeable tsunamis from strike-slip dynamic rupture earthquake  
scenarios on the Húsavík-Flatey Fault Zone. We investigate two distinct fault system geometries to represent the 100 km  
long Húsavík-Flatey Fault Zone striking from onshore to offshore. Our study showcases how dynamic earthquake source  
mechanisms, including dynamic rupture rake rotation near the surface (of  $\pm 20^\circ$ ) combined with large shallow fault slip (up  
to  $\sim 8$  m), cause coseismic vertical displacement in the order of  $\pm 1$  m and the generation of high-amplitude acoustic waves  
420 without strong bathymetric slopes. We find that our earthquake-tsunami scenarios on a less segmented fault system, in particular  
with a hypocenter in the East near the town of Húsavík, generate the largest wave heights of  $\sim 0.9$  m near the local community  
Ólafsfjörður. Húsavík is the only town that is more affected by a scenario with a hypocenter in the West of the HFFZ, causing  
a maximum tsunami crest-to-trough difference of  $\sim 0.4$  m. None of our scenarios regardless of the source complexity endanger  
the town Akureyri, which is shielded by its narrow Eyjafjörður Fjord from the coseismically sourced tsunami. 3D fully-coupled  
425 scenarios include source dynamics, seismic, acoustic, and tsunami waves and result in complexities not present in the one-way  
linked simulations. We observe the excitation of tsunami normal dispersion and unexpectedly large acoustic waves, which  
may serve as a rapid indicator of surface-breaking dynamic rupture. Our findings highlight the importance of considering  
tsunamigenic strike-slip earthquakes in tsunami hazard assessment. Accounting for the dynamics of earthquake source effects  
and fully-coupled tsunami generation may be useful to enhance tsunami hazard assessment and facilitate improvements to  
430 early warning systems.

<https://doi.org/10.5194/egusphere-2023-1262>

Preprint. Discussion started: 30 June 2023

© Author(s) 2023. CC BY 4.0 License.



*Code and data availability.* SeisSol is available from GitHub (<https://github.com/SeisSol>), sam(oa)<sup>2</sup>-flash from GitLab (<https://gitlab.lrz.de/samoa/samoa>). The input files are hosted on Zenodo under <https://zenodo.org/record/8021690>.

*Video supplement.* Supplementary videos showing the propagation of the rupture front together with the seismic wavefield spreading across the surface are available (<https://zenodo.org/record/8021690>). Also included are movies for the tsunami propagation for scenario Simple-East  
435 based on both the one-way linked and fully-coupled method.





## Appendix A: Earthquake dynamic rupture

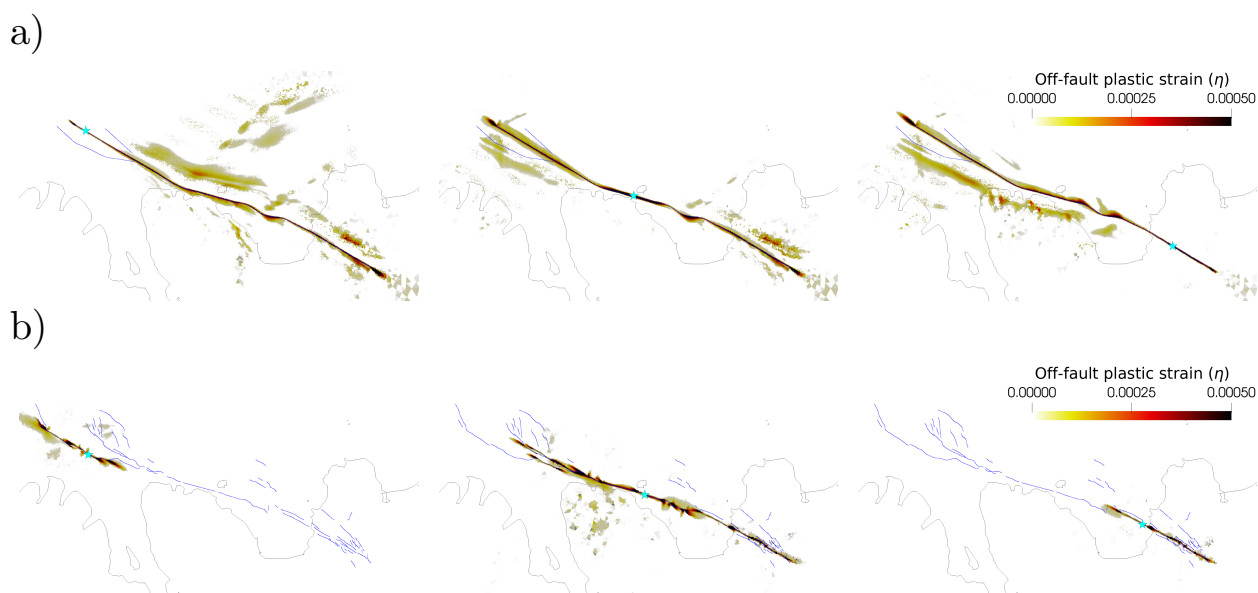
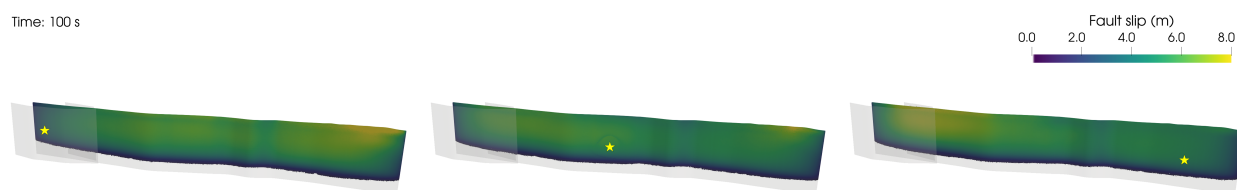


**Figure A1.** Accumulation of off-fault plastic strain ( $\eta$ ) on the free surface for the dynamic rupture simulations on a) the simple fault geometry and b) the complex fault geometry. Cyan stars mark the epicenter locations.



a)

Time: 100 s



b)

Time: 100 s

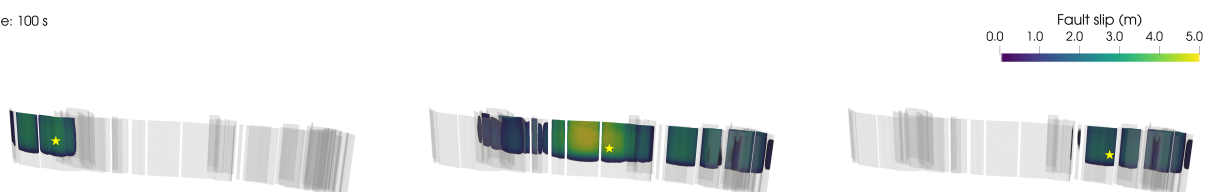


**Figure A2.** Absolute fault slip of the earthquake dynamic rupture simulations on a) the simple fault geometry and b) the complex fault geometry. Yellow stars mark the hypocenter locations. Note the adjusted scale for fault slip in b) to better perceive differences among the three complex scenarios.

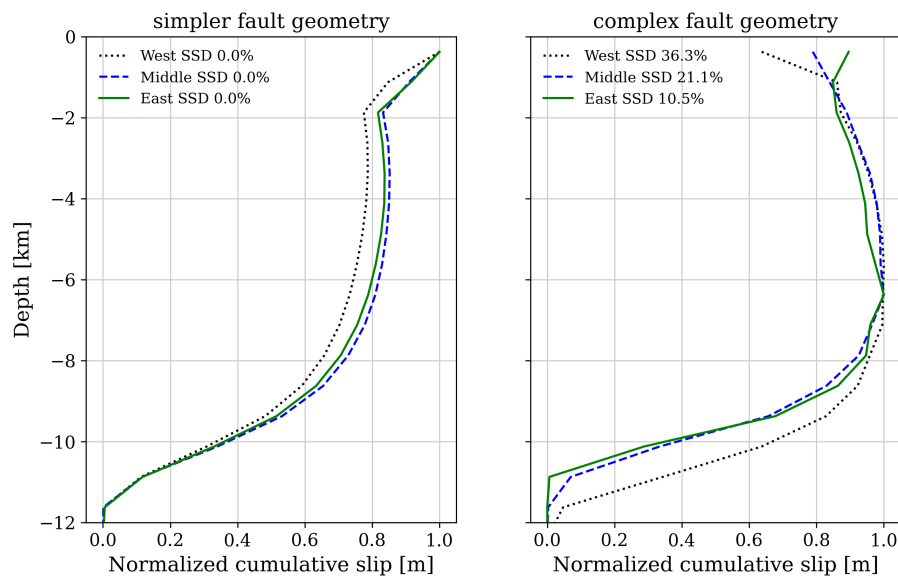


**Figure A3.** Normalized cumulative slip with depth for all six earthquake dynamic ruptures. The amount of shallow slip deficit (SSD) is indicated at the top left for each model on the respective fault geometry. The scenarios on the simpler fault geometry exhibit no SSD with large shallow fault slip, while SSD up to 36.3 % can be observed for dynamic rupture model Complex-West.



## Appendix B: Tsunami

440 sam(oa)<sup>2</sup>-flash takes the time-dependent (only vertical) seafloor displacement as input for the tsunami simulations (Sect. 2.4). Here, a Tanioka filter (Tanioka and Satake, 1996) is applied when converting the SeisSol ground displacement output to the input for sam(oa)<sup>2</sup>-flash. This allows to add the contribution of the horizontal deformation to the vertical displacement, which is, however, very small. Eq. B1 contains the bathymetry  $B$  (positive in the downward direction), the vertical (total) displacement  $u_z$  (and  $u_z^{total}$ ), and the horizontal bathymetric displacement  $u_x$  and  $u_y$ . Subscripts do not denote partial derivatives but solely the respective directions.

$$u_z^{total} = u_z + u_B = u_z + u_x \frac{\partial B}{\partial x} + u_y \frac{\partial B}{\partial y} \quad (\text{B1})$$



### Ssha recordings at synthetic tide gauge stations for complex scenarios

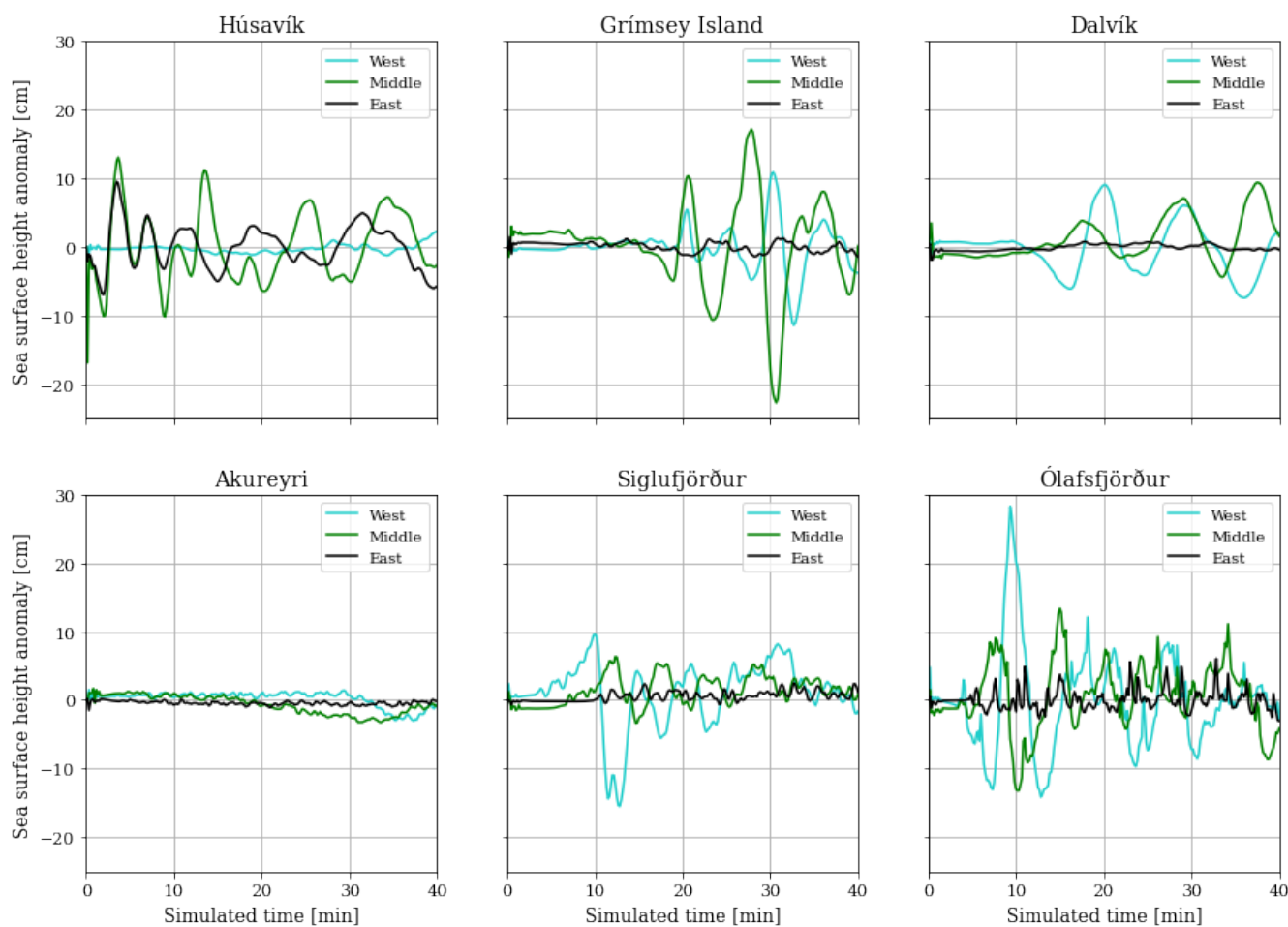


**Figure B1.** Sea surface height anomaly (ssha [cm]) vs simulation time (40 min) for three one-way-linked scenarios sourced by dynamic rupture simulations on the complex fault geometry recorded at six synthetic tide gauge stations close to the towns Húsavík, Akureyri, Dalvík, Ólafsfjörður, Siglufjörður and Grímsey Island.

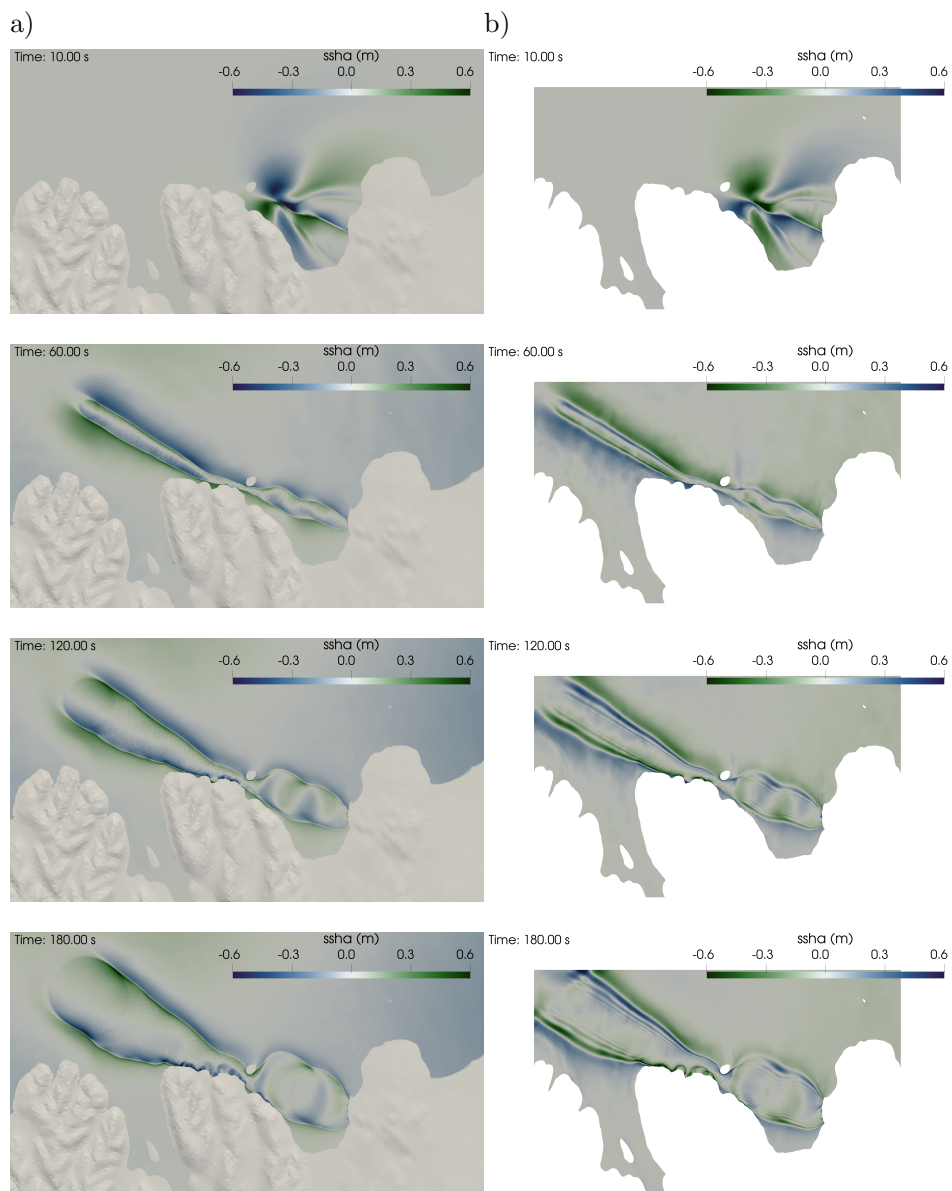


**Figure B2.** Comparison for scenario Simple-East. a) One-way linked simulation. b) Fully-coupled model. Snapshots at 10 s, 1 min, 2 min and 3 min.



### Simple-East

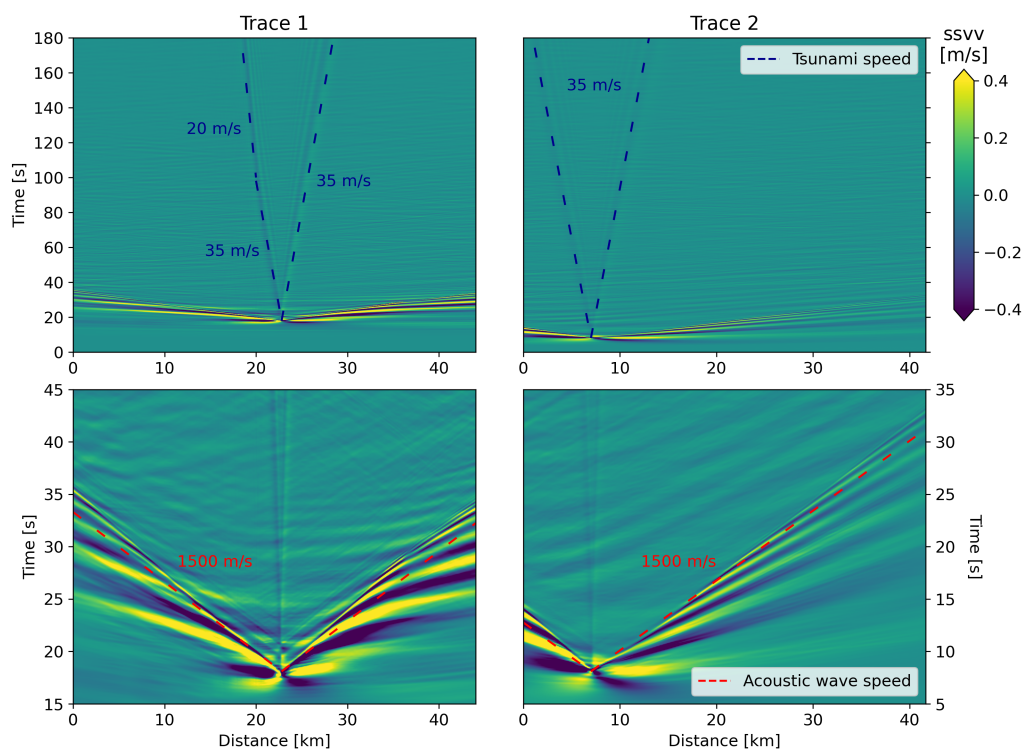


**Figure B3.** Enlarged space-time relationship of the sea surface vertical velocity (ssvv) along two cross-sections for the fully-coupled scenario Simple-East with the gravitational ocean waves and acoustic waves annotated (cf. Fig. 10). The shoreline is located at 0 km. Visible is the relatively constant tsunami speed of  $\sim 35 \text{ m s}^{-1}$ , with which the tsunami propagates towards the open ocean. At the same time, the tsunami front in cross-section 1 moving towards the coast experiences a reduction in velocity (to  $\sim 20 \text{ m s}^{-1}$ ) due to the water depth getting shallower. The upper two rows show the entire simulation time of 3 min. Note the different axis for the lower two rows, which provide zooms into the initial tsunami generation.



### Simple-Middle

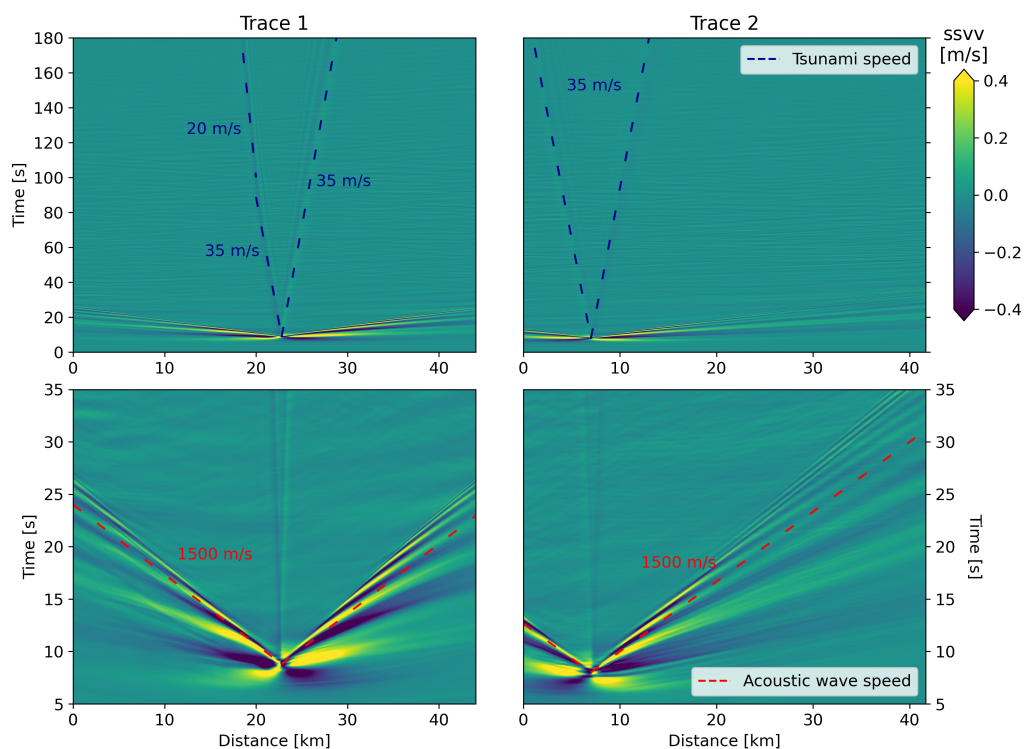


**Figure B4.** Enlarged space-time relationship of the sea surface vertical velocity (ssvv) along two cross-sections for the fully-coupled scenario Simple-Middle with the gravitational ocean waves and acoustic waves annotated (cf. Fig. 11). The shoreline is located at 0 km. The relatively constant tsunami speed of  $\sim 35 \text{ m s}^{-1}$  is visible, with which the tsunami propagates towards the open ocean. At the same time, the tsunami front in cross-section 1 moving towards the coast experiences a reduction in velocity (to  $\sim 20 \text{ m s}^{-1}$ ) due to the decreasing water depth. The upper two rows show the entire simulation time of 3 min. Note the different axis for the lower two rows, which provide zooms into the initial tsunami generation.





### Simple-West

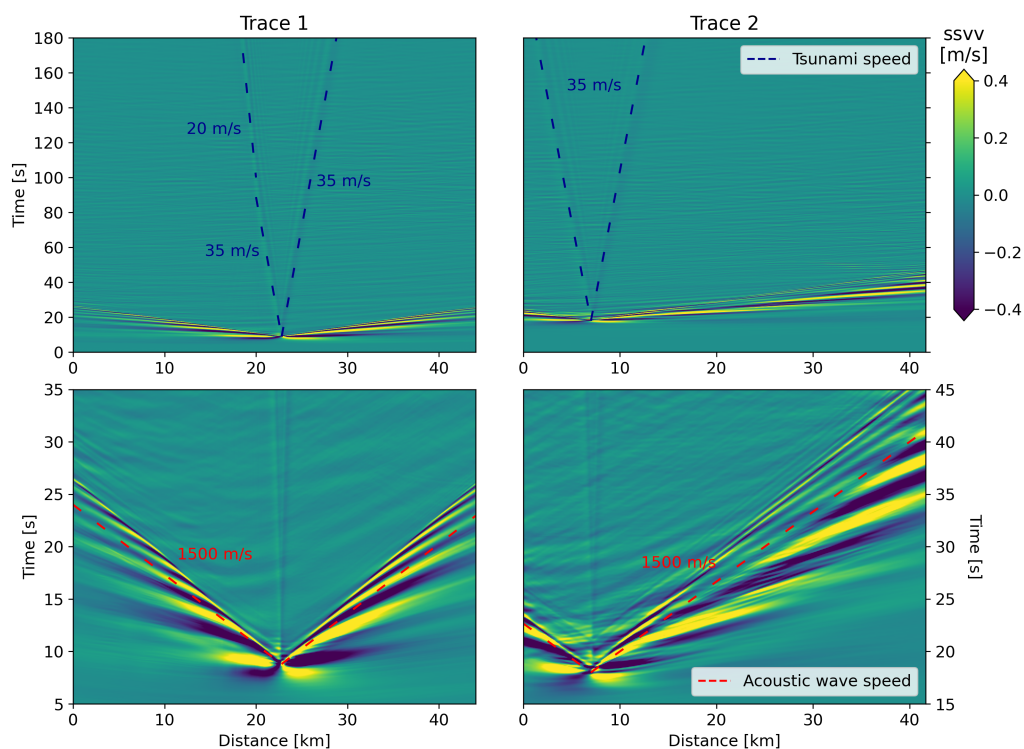


**Figure B5.** Enlarged space-time relationship of the sea surface vertical velocity (ssvv) along two cross-sections for the fully-coupled scenario Simple-West with the gravitational ocean waves and acoustic waves annotated (cf. Fig. 12). The shoreline is located at 0 km. Visible is the relatively constant tsunami speed of  $\sim 35 \text{ m s}^{-1}$ , with which the tsunami propagates towards the open ocean. At the same time, the tsunami front in cross-section 1 moving towards the coast experiences a reduction in velocity (to  $\sim 20 \text{ m s}^{-1}$ ) due to the water depth getting shallower. The upper two rows show the entire simulation time of 3 min. Note the different axis for the lower two rows, which provide zooms into the initial tsunami generation.



445 *Author contributions.* FK performed the formal analysis and used the dynamic rupture (DR) models provided by BL for earthquake-tsunami modeling. FK proceeded with the visualization and writing of the original draft. A-AG supervised the project and gave substantial feedback for conceptualizing the research goals. SW and TU helped in the tsunami model setup and provided their expertise in post-processing earthquake-tsunami simulations. CA provided the dataset of relocated seismicity up to 2019, the 3D velocity model for TFZ, and the simplified fault geometry on the basis of her analyses. Both A-AG and BH acquired financial support. BH further supervised the work done  
450 at IMO. A-AG, BL, SW, TU and BH all provided comments on the manuscript and helped to review & edit the original draft. Each author contributed to the article and approved the submitted version.

*Competing interests.* The authors declare that they have no conflict of interest.

*Acknowledgements.* This work received funding from the European Union's Horizon 2020 research and innovation programme (TEAR ERC Starting grant agreement No. 852992) and Horizon Europe (ChEESE-2P grant No. 101093038, DT-GEO grant No. 101058129 and Geo-  
455 INQUIRE grant No. 101058518). We acknowledge additional funding from the National Science Foundation (grant No. EAR-2121666) and the National Aeronautics and Space Administration (80NSSC20K0495). We thank Lukas Krenz, Lauren Abrahams and Eric Dunham for invaluable discussions and their contributions to the 3D fully-coupled earthquake-tsunami modeling capabilities in SeisSol. We thank all participants of the NorthQuake 2022 workshop (<https://hac.is/en/radstefnur/northquake-2022>) for insightful presentations and discussions. The computing infrastructure available at the Department of Earth and Environmental Sciences at LMU, Geophysics (Oeser et al., 2006), and  
460 at the Leibniz Supercomputing Center (LRZ, projects no. pn68fi, pr63qo, and pn49ha) are highly appreciated. The Generic Mapping Tools (Wessel et al., 2019) and its Python interface PyGMT (Uieda et al., 2022) were used to generate some of the figures. We used two kinds of gridded bathymetric data (Ryan et al., 2009; GEBCO Compilation Group, 2020) and scientific colour maps (Crameri, 2018; Crameri et al., 2020).



## References

- 465 Abrahams, L. S., Krenz, L., Dunham, E. M., Gabriel, A.-A., and Saito, T.: Comparison of methods for coupled earthquake and tsunami modelling, *Geophysical Journal International*, 234, 404–426, <https://doi.org/10.1093/GJI/GGAD053>, 2023.
- Abril, C., Gudmundsson, O., and the SIL seismological group: Relocating earthquakes with empirical traveltimes, *Geophysical Journal International*, 214, 2098–2114, <https://doi.org/10.1093/GJI/GGY246>, 2018.
- Abril, C., Gudmundsson, O., and Tryggvason, A.: Earthquake Relocation in the Tjörnes Fracture Zone, in: *Proceedings of the Northquake 2019 workshop* (Ed. S. Jónsson et al.), pp. 37–40, Húsavík Academic Centre, 2019.
- 470 Abril, C., Tryggvason, A., Gudmundsson, and Steffen, R.: Local Earthquake Tomography in the Tjörnes Fracture Zone (North Iceland), *Journal of Geophysical Research: Solid Earth*, 126, e2020JB020212, <https://doi.org/10.1029/2020JB020212>, 2021.
- Aki, K. and Richards, P. G.: *Quantitative Seismology*, University Science Books, 2nd edn., 2002.
- Ambraseys, N. and Sigbjörnsson, R.: Re-appraisal of the seismicity of Iceland, *Polytechnica – Engineering Seismology*, 3, 183, 2000.
- 475 Amlani, F., Bhat, H. S., Simons, W. J., Schubnel, A., Vigny, C., Rosakis, A. J., Efendi, J., Elbanna, A. E., Dubernet, P., and Abidin, H. Z.: Supershear shock front contribution to the tsunami from the 2018 Mw 7.5 Palu, Indonesia earthquake, *Geophysical Journal International*, 230, 2089–2097, <https://doi.org/10.1093/GJI/GGAC162>, 2022.
- Anderson, E. M.: The dynamics of faulting, *Transactions of the Edinburgh Geological Society*, 8, 387–402, <https://doi.org/10.1144/TRANSED.8.3.387>, 1905.
- 480 Andrews, D. J.: Rupture velocity of plane strain shear cracks, *Journal of Geophysical Research*, 81, 5679–5687, <https://doi.org/10.1029/JB081I032P05679>, 1976.
- Angelier, J., Slunga, R., Bergerat, F., Stefansson, R., and Homberg, C.: Perturbation of stress and oceanic rift extension across transform faults shown by earthquake focal mechanisms in Iceland, *Earth and Planetary Science Letters*, 219, 271–284, [https://doi.org/10.1016/S0012-821X\(03\)00704-0](https://doi.org/10.1016/S0012-821X(03)00704-0), 2004.
- 485 Antoine, S. L., Klinger, Y., Delorme, A., and Gold, R. D.: Off-fault deformation in regions of complex fault geometries: The 2013, Mw7.7, Baluchistan rupture (Pakistan), *Journal of Geophysical Research: Solid Earth*, p. e2022JB024480, <https://doi.org/10.1029/2022JB024480>, 2022.
- Aochi, H. and Ulrich, T.: A Probable Earthquake Scenario near Istanbul Determined from Dynamic Simulations, *Bulletin of the Seismological Society of America*, 105, 1468–1475, <https://doi.org/10.1785/0120140283>, 2015.
- 490 Baba, T., Chikasada, N., Imai, K., Tanioka, Y., and Kodaira, S.: Frequency dispersion amplifies tsunamis caused by outer-rise normal faults, *Scientific Reports*, 11, 1–11, <https://doi.org/10.1038/s41598-021-99536-x>, 2021.
- Bao, H., Ampuero, J. P., Meng, L., Fielding, E. J., Liang, C., Milliner, C. W., Feng, T., and Huang, H.: Early and persistent supershear rupture of the 2018 magnitude 7.5 Palu earthquake, *Nature Geoscience*, 12, 200–205, <https://doi.org/10.1038/s41561-018-0297-z>, 2019.
- Barreto, A., Viltres, R., Matrau, R., Ófeigsson, B. G., and Jónsson, S.: Insights into Two Decades of continuous and Campaign GPS Data in North Iceland, in: *Proceedings of the NorthQuake 2022 workshop* (Ed. S. Jónsson et al.), pp. 11–13, Húsavík Academic Centre, 2022.
- 495 Ben-Zion, Y., Peng, Z., Okaya, D., Seeber, L., Armbruster, J. G., Ozer, N., Michael, A. J., Baris, S., and Aktar, M.: A shallow fault-zone structure illuminated by trapped waves in the Karadere-Duzce branch of the North Anatolian Fault, western Turkey, *Geophysical Journal International*, 152, 699–717, <https://doi.org/10.1046/j.1365-246X.2003.01870.x>, 2003.
- Ben-Zion, Y., Beroza, G. C., Bohnhoff, M., Gabriel, A., and Mai, P. M.: A Grand Challenge International Infrastructure for Earthquake Science, *Seismological Research Letters*, 93, 2967–2968, <https://doi.org/10.1785/0220220266>, 2022.
- 500



- Bernard, E. and Titov, V.: Evolution of tsunami warning systems and products, *Philosophical Transactions of the Royal Society A: Mathematical, Physical and Engineering Sciences*, 373, <https://doi.org/10.1098/RSTA.2014.0371>, 2015.
- Biemiller, J., Gabriel, A. A., and Ulrich, T.: The Dynamics of Unlikely Slip: 3D Modeling of Low-Angle Normal Fault Rupture at the Mai'iu Fault, Papua New Guinea, *Geochemistry, Geophysics, Geosystems*, 23, e2021GC010298, <https://doi.org/10.1029/2021GC010298>, 2022.
- 505 Biemiller, J., Gabriel, A.-A., and Ulrich, T.: Dueling dynamics of low-angle normal fault rupture with splay faulting and off-fault damage, *Nature Communications*, 14, 1–12, <https://doi.org/10.1038/s41467-023-37063-1>, 2023.
- Bilek, S. and Lay, T.: Subduction zone megathrust earthquakes, *Geosphere*, 14, <https://doi.org/10.1130/GES01608.1>, 2018.
- Brandsdóttir, B., Riedel, C., Richter, B., Helgadóttir, G., Kjartansson, E., Detrick, R., Dahm, T., Mayer, L., Calder, B., and Driscoll, N.: Multibeam bathymetric maps of the Kolbeinsey Ridge and Tjörnes Fracture Zone, N-Iceland, European Geosciences Union, <https://meetings.copernicus.org/www.cosis.net/abstracts/EGU05/07219/EGU05-J-07219.pdf>, 2005.
- 510 Brandsdóttir, B., Detrick, R. S., Driscoll, N. W., Karson, J. A., Guðmundsson, G. B., and Jónsdóttir, K.: Postglacial faulting within the Skjálfandi Bay, in: *Proceedings of the NorthQuake 2022 workshop* (Ed. S. Jónsson et al.), pp. 10–10, Húsavík Academic Centre, 2022.
- Breuer, A., Heinecke, A., Rannabauer, L., and Bader, M.: High-order ADER-DG minimizes energy- and time-to-solution of SeisSol, *Lecture Notes in Computer Science (including subseries Lecture Notes in Artificial Intelligence and Lecture Notes in Bioinformatics)*, 9137 LNCS, 515 340–357, [https://doi.org/10.1007/978-3-319-20119-1\\_25](https://doi.org/10.1007/978-3-319-20119-1_25), 2015.
- Byerlee, J.: Friction of rocks, *pure and applied geophysics* 1978 116:4, 116, 615–626, <https://doi.org/10.1007/BF00876528>, 1978.
- Cecioni, C., Bellotti, G., Romano, A., Abdolali, A., Sammarco, P., and Franco, L.: Tsunami Early Warning System based on Real-time Measurements of Hydro-acoustic Waves, *Procedia Engineering*, 70, 311–320, <https://doi.org/10.1016/J.PROENG.2014.02.035>, 2014.
- Célérier, B.: Seeking Anderson's faulting in seismicity: A centennial celebration, *Reviews of Geophysics*, 46, 4001, 520 <https://doi.org/10.1029/2007RG000240>, 2008.
- Celli, N. L., Lebedev, S., Schaeffer, A. J., and Gaina, C.: The tilted Iceland Plume and its effect on the North Atlantic evolution and magmatism, *Earth and Planetary Science Letters*, 569, 117 048, <https://doi.org/10.1016/J.EPSL.2021.117048>, 2021.
- Coulomb, C. A.: Essai sur une application des règles des maximise et minimis a quelque problèmes de statique, *Mémoire Académie Royale des Sciences*, 7, 1776.
- 525 Cramer, F.: Scientific colour maps, *Zenodo*, <https://doi.org/10.5281/zenodo.1243862>, 2018.
- Cramer, F., Shephard, G. E., and Heron, P. J.: The misuse of colour in science communication, *Nature Communications*, 11, 1–10, <https://doi.org/10.1038/s41467-020-19160-7>, 2020.
- de la Puente, J., Ampuero, J.-P., and Käser, M.: Dynamic rupture modeling on unstructured meshes using a discontinuous Galerkin method, *Journal of Geophysical Research: Solid Earth*, 114, <https://doi.org/10.1029/2008JB006271>, 2009.
- 530 De Pascale, G. P.: Húsavík-Flatey fault behavior and outstanding data gaps based on insight from major strike slip faults, in: *Proceedings of the NorthQuake 2022 workshop* (Ed. S. Jónsson et al.), Húsavík Academic Centre, 2022.
- Demets, C., Gordon, R., and Argus, D.: Geological current plate motions, *Geophysical Journal International*, 181, 1–80, <https://doi.org/10.1111/j.1365-246X.2009.04491.x>, 2010.
- Douilly, R., Aochi, H., Calais, E., and Freed, A. M.: Three-dimensional dynamic rupture simulations across interacting faults: The Mw7.0, 535 2010, Haiti earthquake, *Journal of Geophysical Research: Solid Earth*, 120, 1108–1128, <https://doi.org/10.1002/2014JB011595>, 2015.
- Dumbser, M. and Käser, M.: An Arbitrary High Order Discontinuous Galerkin Method for Elastic Waves on Unstructured Meshes II: The Three-Dimensional Isotropic Case, *Geophysical Journal International*, 167, 319–336, <https://doi.org/10.1111/j.1365-246X.2006.03120.x>, 2006.



- 540 Einarsson, P.: Earthquakes and present-day tectonism in Iceland, *Tectonophysics*, 189, 261–279, [https://doi.org/10.1016/0040-1951\(91\)90501-I](https://doi.org/10.1016/0040-1951(91)90501-I), 1991.
- Einarsson, P.: Plate boundaries, rifts and transforms in Iceland, *Jokull*, 58, 35–58, <https://doi.org/10.33799/jokull2008.58.035>, 2008.
- Einarsson, P. and Brandsdóttir, B.: Seismicity of the Northern Volcanic Zone of Iceland, *Frontiers in Earth Science*, 9, 166, <https://doi.org/10.3389/feart.2021.628967>, 2021.
- 545 Elbanna, A., Abdelmeguid, M., Ma, X., Amlani, F., Bhat, H. S., Synolakis, C., and Rosakis, A. J.: Anatomy of strike-slip fault tsunami genesis, *Proceedings of the National Academy of Sciences of the United States of America*, 118, 2025632118, <https://doi.org/10.1073/pnas.2025632118>, 2021.
- Fialko, Y., Sandwell, D., Simons, M., and Rosen, P.: Three-dimensional deformation caused by the Bam, Iran, earthquake and the origin of shallow slip deficit, *Nature*, 435, 295–299, <https://doi.org/10.1038/nature03425>, 2005.
- Garcia, S. and Dhont, D.: Structural analysis of the Húsavík-Flatey Transform Fault and its relationships with the rift system in Northern 550 Iceland, *Geodinamica Acta*, 18, 31–41, <https://doi.org/10.3166/GA.18.31-41>, 2004.
- GEBCO Compilation Group: GEBCO 2020 Grid, <https://doi.org/10.5285/a29c5465-b138-234d-e053-6c86abc040b9>, 2020.
- Geirsson, H., Árnadóttir, T., Völksen, C., Jiang, W., Sturkell, E., Villemin, T., Einarsson, P., Sigmundsson, F., and Stefánsson, R.: Current plate movements across the Mid-Atlantic Ridge determined from 5 years of continuous GPS measurements in Iceland, *Journal of Geophysical Research: Solid Earth*, 111, <https://doi.org/10.1029/2005JB003717>, 2006.
- 555 Glimsdal, S., Pedersen, G. K., Harbitz, C. B., and Løvholt, F.: Dispersion of tsunamis: does it really matter?, *Natural Hazards and Earth System Sciences*, 13, 1507–1526, <https://doi.org/10.5194/NHESS-13-1507-2013>, 2013.
- Gomez, B. and Kadri, U.: Near real-time calculation of submarine fault properties using an inverse model of acoustic signals, *Applied Ocean Research*, 109, 102557, <https://doi.org/10.1016/J.APOR.2021.102557>, 2021.
- Harbitz, C. B., Løvholt, F., Pedersen, G., and Masson, D. G.: Mechanisms of tsunami generation by submarine landslides: a short review, 560 *Norwegian Journal of Geology*, 86, 255–264, 2006.
- Harrington, J., Avsar, U., Klinger, Y., Jónsson, S., and Gudmundsdóttir, E. R.: Fault trenching and geologic slip rates of the Húsavík-Flatey Fault, North Iceland, in: *Proceedings of the 2nd workshop on Earthquakes in North Iceland* (Ed. R. Stefánsson et al.), pp. 24–26, Húsavík Academic Centre, Húsavík, [https://www.hac.is/wp-content/uploads/2016/04/Conpro\\_webfinal.compressed.pdf#page=26](https://www.hac.is/wp-content/uploads/2016/04/Conpro_webfinal.compressed.pdf#page=26), 2016.
- Harris, R. A., Aagaard, B., Barall, M., Ma, S., Roten, D., Olsen, K., Duan, B., Liu, D., Luo, B., Bai, K., Ampuero, J. P., Kaneko, Y., Gabriel, 565 A. A., Duru, K., Ulrich, T., Wollherr, S., Shi, Z., Dunham, E., Bydlon, S., Zhang, Z., Chen, X., Somala, S. N., Pelties, C., Tago, J., Cruz-Atienza, V. M., Kozdon, J., Daub, E., Aslam, K., Kase, Y., Withers, K., and Dalguer, L.: A suite of exercises for verifying dynamic earthquake rupture codes, *Seismological Research Letters*, 89, 1146–1162, <https://doi.org/10.1785/0220170222>, 2018.
- Harris, R. A., Barall, M., Lockner, D. A., Moore, D. E., Ponce, D. A., Graymer, R. W., Funning, G., Morrow, C. A., Kyriakopoulos, C., and Eberhart-Phillips, D.: A Geology and Geodesy Based Model of Dynamic Earthquake Rupture on the Rodgers Creek-Hayward-Calaveras 570 Fault System, California, *Journal of Geophysical Research: Solid Earth*, 126, e2020JB020577, <https://doi.org/10.1029/2020JB020577>, 2021.
- Heidbach, O., Reinecker, J., Tingay, M., Müller, B., Sperner, B., Fuchs, K., and Wenzel, F.: Plate boundary forces are not enough: Second- and third-order stress patterns highlighted in the World Stress Map database, *Tectonics*, 26, <https://doi.org/10.1029/2007TC002133>, 2007.
- Heidbach, O., Tingay, M., Barth, A., Reinecker, J., Kurfeß, D., and Müller, B.: Global crustal stress pattern based on the World Stress Map 575 database release 2008, *Tectonophysics*, 482, 3–15, <https://doi.org/10.1016/J.TECTO.2009.07.023>, 2010.



- Hjartardóttir, A. R., Einarsson, P., Magnúsdóttir, S., Björnsdóttir, T., and Brandsdóttir, B.: Fracture systems of the Northern Volcanic Rift Zone, Iceland: An onshore part of the Mid-Atlantic plate boundary, *Geological Society Special Publication*, 420, 297–314, <https://doi.org/10.1144/SP420.1>, 2016.
- Hjartarson, A., Erlendsson, O., and Blischke, A.: The Greenland-Iceland-Faroe Ridge complex, *Geological Society Special Publication*, 447, 127–148, <https://doi.org/10.1144/SP447.14>, 2017.
- 580 Ida, Y.: Cohesive force across the tip of a longitudinal-shear crack and Griffith's specific surface energy, *Journal of Geophysical Research*, 77, 3796–3805, <https://doi.org/10.1029/JB077I020P03796>, 1972.
- Jiao, L., Klinger, Y., and Scholtès, L.: Fault Segmentation Pattern Controlled by Thickness of Brittle Crust, *Geophysical Research Letters*, 48, e2021GL093390, <https://doi.org/10.1029/2021GL093390>, 2021.
- 585 Jónsson, S.: Do large Earthquakes in North Iceland usually occur in Winter?, in: *Proceedings of the Northquake 2019 workshop* (Ed. S. Jónsson et al.), pp. 45–48, Húsvík Academic Centre, 2019.
- Kanamori, H.: Mechanism of tsunami earthquakes, *Physics of the Earth and Planetary Interiors*, 6, 346–359, [https://doi.org/10.1016/0031-9201\(72\)90058-1](https://doi.org/10.1016/0031-9201(72)90058-1), 1972.
- Kaneko, Y. and Goto, H.: The Origin of Large, Long-Period Near-Fault Ground Velocities During Surface-Breaking Strike-Slip Earthquakes, *Geophysical Research Letters*, 49, e2022GL098029, <https://doi.org/10.1029/2022GL098029>, 2022.
- 590 Karson, J. A., Farrell, J. A., Chutas, L. A., Nanfito, A. F., Proett, J. A., Runnals, K. T., and Sæmundsson, K.: Rift-Parallel Strike-Slip Faulting Near the Iceland Plate Boundary Zone: Implications for Propagating Rifts, *Tectonics*, 37, 4567–4594, <https://doi.org/10.1029/2018TC005206>, 2018.
- Käser, M. and Dumbser, M.: An arbitrary high-order discontinuous Galerkin method for elastic waves on unstructured meshes - I. The two-dimensional isotropic case with external source terms, *Geophysical Journal International*, 166, 855–877, <https://doi.org/10.1111/j.1365-246X.2006.03051.x>, 2006.
- 595 Kearse, J. and Kaneko, Y.: On-Fault Geological Fingerprint of Earthquake Rupture Direction, *Journal of Geophysical Research: Solid Earth*, 125, e2020JB019863, <https://doi.org/10.1029/2020JB019863>, 2020.
- Kearse, J., Kaneko, Y., Little, T., and Van Dissen, R.: Curved slickenlines preserve direction of rupture propagation, *Geology*, 47, 838–842, <https://doi.org/10.1130/G46563.1>, 2019.
- 600 Klinger, Y.: Relation between continental strike-slip earthquake segmentation and thickness of the crust, *Journal of Geophysical Research: Solid Earth*, 115, 7306, <https://doi.org/10.1029/2009JB006550>, 2010.
- Klinger, Y.: Imprint of the Continental Strike-Slip Fault Geometrical Structure in Geophysical Data, *Geophysical Research Letters*, 49, e2022GL098146, <https://doi.org/10.1029/2022GL098146>, 2022.
- 605 Kowsari, M., Sonnemann, T., Halldórsson, B., Hrafnkelsson, B., Snæbjörnsson, J., and Jónsson, S.: Bayesian inference of empirical ground motion models to pseudo-spectral accelerations of south Iceland seismic zone earthquakes based on informative priors, *Soil Dynamics and Earthquake Engineering*, 132, 106075, <https://doi.org/10.1016/J.SOILDYN.2020.106075>, 2020.
- Krenz, L., Uphoff, C., Ulrich, T., Gabriel, A. A., Abrahams, L. S., Dunham, E. M., and Bader, M.: 3D Acoustic-Elastic Coupling with Gravity: The Dynamics of the 2018 Palu, Sulawesi Earthquake and Tsunami, *International Conference for High Performance Computing, Networking, Storage and Analysis, SC*, <https://doi.org/10.1145/3458817.3476173>, 2021.
- 610 Krenz, L., Wolf, S., Hillers, G., Gabriel, A.-A., and Bader, M.: Numerical simulations of seismo-acoustic nuisance patterns from an induced M1.8 earthquake in the Helsinki, southern Finland, metropolitan area, *arXiv*, <https://arxiv.org/abs/2211.03647v2>, 2023.



- Kyriakopoulos, C., Oglesby, D. D., Funning, G. J., and Ryan, K. J.: Dynamic Rupture Modeling of the M7.2 2010 El Mayor-Cucapah Earthquake: Comparison With a Geodetic Model, *Journal of Geophysical Research: Solid Earth*, 122, 263–10, 615 <https://doi.org/10.1002/2017JB014294>, 2017.
- Lefevre, M., Souloumiac, P., Cubas, N., and Klinger, Y.: Experimental evidence for crustal control over seismic fault segmentation, *Geology*, 48, 844–848, <https://doi.org/10.1130/G47115.1>, 2020.
- Li, B., Wu, B., Bao, H., Oglesby, D. D., Ghosh, A., Gabriel, A.-A., Meng, L., and Chu, R.: Rupture Heterogeneity and Directivity Effects in Back-Projection Analysis, *Journal of Geophysical Research: Solid Earth*, 127, e2021JB022 663, <https://doi.org/10.1029/2021JB022663>, 620 2022.
- Li, B., Gabriel, A.-A., Ulrich, T., Abril, C., and Halldorsson, B.: Dynamic Rupture Models, Fault Interaction and Ground Motion Simulations for the Segmented Húsavík-Flatey Fault Zone, Northern Iceland, *Journal of Geophysical Research: Solid Earth*, 128, e2022JB025 886, <https://doi.org/10.1029/2022JB025886>, 2023.
- Lotto, G. C. and Dunham, E. M.: High-order finite difference modeling of tsunami generation in a compressible ocean from offshore earthquakes, *Computational Geosciences*, 19, 327–340, <https://doi.org/10.1007/S10596-015-9472-0>, 2015.
- Lotto, G. C., Jeppson, T. N., and Dunham, E. M.: Fully Coupled Simulations of Megathrust Earthquakes and Tsunamis in the Japan Trench, Nankai Trough, and Cascadia Subduction Zone, *Pure and Applied Geophysics*, 176, 4009–4041, <https://doi.org/10.1007/S00024-018-1990-Y>, 2018.
- Løvholt, F., Pedersen, G., Harbitz, C. B., Glimsdal, S., and Kim, J.: On the characteristics of landslide tsunamis, *Philosophical Transactions of the Royal Society A: Mathematical, Physical and Engineering Sciences*, 373, <https://doi.org/10.1098/RSTA.2014.0376>, 2015.
- Lozos, J. C. and Harris, R. A.: Dynamic Rupture Simulations of the M6.4 and M7.1 July 2019 Ridgecrest, California, Earthquakes, *Geophysical Research Letters*, 47, e2019GL086 020, <https://doi.org/10.1029/2019GL086020>, 2020.
- Ma, S.: A physical model for widespread near-surface and fault zone damage induced by earthquakes, *Geochemistry, Geophysics, Geosystems*, 9, 11 009, <https://doi.org/10.1029/2008GC002231>, 2008.
- 635 Ma, S.: Dynamic off-fault failure and tsunamigenesis at strike-slip restraining bends: Fully-coupled models of dynamic rupture, ocean acoustic waves, and tsunami in a shallow bay, *Tectonophysics*, 838, 229 496, <https://doi.org/10.1016/J.TECTO.2022.229496>, 2022.
- Ma, S. and Andrews, D. J.: Inelastic off-fault response and three-dimensional dynamics of earthquake rupture on a strike-slip fault, *Journal of Geophysical Research: Solid Earth*, 115, 4304, <https://doi.org/10.1029/2009JB006382>, 2010.
- Ma, S. and Nie, S.: Dynamic Wedge Failure and Along-Arc Variations of Tsunamigenesis in the Japan Trench Margin, *Geophysical Research Letters*, 46, 8782–8790, <https://doi.org/10.1029/2019GL083148>, 2019.
- 640 Madariaga, R., Ampuero, J. P., and Adda-Bedia, M.: Seismic Radiation from Simple Models of Earthquakes, in: *Earthquakes: Radiated Energy and the Physics of Faulting*, pp. 223–236, American Geophysical Union (AGU), <https://doi.org/10.1029/170GM23>, 2006.
- Madden, E. H., Bader, M., Behrens, J., Van Dinther, Y., Gabriel, A. A., Rannabauer, L., Ulrich, T., Uphoff, C., Vater, S., and Van Zelst, I.: 645 Linked 3-D modelling of megathrust earthquake-tsunami events: from subduction to tsunami run up, *Geophysical Journal International*, 224, 487–516, <https://doi.org/10.1093/GJI/GGAA484>, 2020.
- Maeda, T., Furumura, T., Noguchi, S., Takemura, S., Sakai, S., Shinohara, M., Iwai, K., and Lee, S. J.: Seismic- and Tsunami-Wave Propagation of the 2011 Off the Pacific Coast of Tohoku Earthquake as Inferred from the Tsunami-Coupled Finite-Difference Simulation, *Bulletin of the Seismological Society of America*, 103, 1456–1472, <https://doi.org/10.1785/0120120118>, 2013.
- 650 Magnúsdóttir, S. and Brandsdóttir, B.: Tectonics of the Þeistareykir fissure swarm, *Jökull*, pp. 65–79, 2011.



- Magnúsdóttir, S., Brandsdóttir, B., Driscoll, N., and Detrick, R.: Postglacial tectonic activity within the Skjálfandadjúp Basin, Tjörnes Fracture Zone, offshore Northern Iceland, based on high resolution seismic stratigraphy, *Marine Geology*, 367, 159–170, <https://doi.org/10.1016/J.MARGEO.2015.06.004>, 2015.
- Marchandon, M., Hollingsworth, J., and Radiguet, M.: Origin of the shallow slip deficit on a strike slip fault: Influence of elastic structure, topography, data coverage, and noise, *Earth and Planetary Science Letters*, 554, 116–696, <https://doi.org/10.1016/J.EPSL.2020.116696>, 2021.
- Matrau, R., Klinger, Y., Harrington, J., Avsar, U., Gudmundsdóttir, E. R., Thordarson, T., Hoskuldsson, A., and Jonsson, S.: Paleoearthquakes on the Húsavík-Flatey Fault in northern Iceland: Where are the large earthquakes?, EGU General Assembly, <https://doi.org/10.5194/egusphere-egu21-13998>, 2021.
- 660 Matrau, R., Klinger, Y., Harrington, J., Thordarson, T., Hoskuldsson, A., Gudmundsdóttir, E. R., Parisi, L., Fittipaldi, M., Avsar, U., and Jónsson, S.: Investigating Holocene deformation on the Húsavík Flatey Fault, in: *Proceedings of the NorthQuake 2022 workshop* (Ed. S. Jónsson et al.), pp. 7–9, Húsavík Academic Centre, 2022.
- Mei, C. C. and Kadri, U.: Sound signals of tsunamis from a slender fault, *Journal of Fluid Mechanics*, 836, 352–373, <https://doi.org/10.1017/JFM.2017.811>, 2017.
- 665 Meister, O., Rahnema, K., and Bader, M.: Parallel Memory-Efficient Adaptive Mesh Refinement on Structured Triangular Meshes with Billions of Grid Cells, *ACM Transactions on Mathematical Software (TOMS)*, 43, <https://doi.org/10.1145/2947668>, 2016.
- Melgar, D. and Ruiz-Angulo, A.: Long-Lived Tsunami Edge Waves and Shelf Resonance From the M8.2 Tehuantepec Earthquake, *Geophysical Research Letters*, 45, 414–12, <https://doi.org/10.1029/2018GL080823>, 2018.
- Metzger, S. and Jónsson, S.: Plate boundary deformation in North Iceland during 1992–2009 revealed by InSAR time-series analysis and GPS, *Tectonophysics*, 634, 127–138, <https://doi.org/10.1016/j.tecto.2014.07.027>, 2014.
- 670 Metzger, S., Jónsson, S., and Geirsson, H.: Locking depth and slip-rate of the Húsavík Flatey fault, North Iceland, derived from continuous GPS data 2006–2010, *Geophysical Journal International*, 187, 564–576, <https://doi.org/10.1111/j.1365-246X.2011.05176.x>, 2011.
- Metzger, S., Jónsson, S., Danielsen, G., Hreinsdóttir, S., Jouanne, F., Giardini, D., and Villemin, T.: Present kinematics of the Tjörnes Fracture Zone, North Iceland, from campaign and continuous GPS measurements, *Geophysical Journal International*, 192, 441–455, <https://doi.org/10.1093/gji/ggs032>, 2013.
- 675 Moretti, L., Mangeney, A., Walter, F., Capdeville, Y., Bodin, T., Stutzmann, E., and Le Friant, A.: Constraining landslide characteristics with Bayesian inversion of field and seismic data, *Geophysical Journal International*, 221, 1341–1348, <https://doi.org/10.1093/GJI/GGAA056>, 2020.
- Mori, N., Satake, K., Cox, D., Goda, K., Catalan, P. A., Ho, T.-C., Imamura, F., Tomiczek, T., Lynett, P., Miyashita, T., Muhari, A., Titov, V., and Wilson, R.: Giant tsunami monitoring, early warning and hazard assessment, *Nature Reviews Earth & Environment*, pp. 1–16, <https://doi.org/10.1038/s43017-022-00327-3>, 2022.
- 680 Noguchi, S., Maeda, T., and Furumura, T.: FDM Simulation of an Anomalous Later Phase from the Japan Trench Subduction Zone Earthquakes, *Pure and Applied Geophysics*, 170, 95–108, <https://doi.org/10.1007/S00024-011-0412-1/METRICAL>, 2013.
- Nosov, M. A. and Kolesov, S. V.: Elastic oscillations of water column in the 2003 Tokachi-oki tsunami source: in-situ measurements and 3-D numerical modelling, *Natural Hazards and Earth System Sciences*, 7, 243–249, <https://doi.org/10.5194/nhess-7-243-2007>, 2007.
- 685 Oeser, J., Bunge, H. P., and Mohr, M.: Cluster Design in the Earth Sciences Tethys, *Lecture Notes in Computer Science (including subseries Lecture Notes in Artificial Intelligence and Lecture Notes in Bioinformatics)*, 4208 LNCS, 31–40, [https://doi.org/10.1007/11847366\\_4](https://doi.org/10.1007/11847366_4), 2006.





- Okada, Y.: Surface deformation due to shear and tensile faults in a half-space, *Bulletin of the Seismological Society of America*, 75, 1135–1154, 1985.
- 690 Okuwaki, R., Yagi, Y., and Hirano, S.: Relationship between High-frequency Radiation and Asperity Ruptures, Revealed by Hybrid Back-projection with a Non-planar Fault Model, *Scientific Reports* 2014 4:1, 4, 1–6, <https://doi.org/10.1038/srep07120>, 2014.
- Olsen, K. B., Madariaga, R., and Archuleta, R. J.: Three-Dimensional Dynamic Simulation of the 1992 Landers Earthquake, *Science*, 278, 834–838, <https://doi.org/10.1126/SCIENCE.278.5339.834>, 1997.
- 695 Pelties, C., Gabriel, A.-A., and Ampuero, J.-P.: Verification of an ADER-DG method for complex dynamic rupture problems, *Geoscientific Model Development*, 7, 847–866, <https://doi.org/10.5194/gmd-7-847-2014>, 2014.
- Poulain, P., Le Friant, A., Pedreros, R., Mangeney, A., Filippini, A. G., Grandjean, G., Lemoine, A., Fernández-Nieto, E. D., Castro Díaz, M. J., and Peruzzetto, M.: Numerical simulation of submarine landslides and generated tsunamis: application to the on-going Mayotte seismo-volcanic crisis, *Comptes Rendus - Geoscience*, 354, 361–390, <https://doi.org/10.5802/crgeos.138>, 2022.
- 700 Ramos, M. D., Thakur, P., Huang, Y., Harris, R. A., and Ryan, K. J.: Working with Dynamic Earthquake Rupture Models: A Practical Guide, *Seismological Research Letters*, 93, 2096–2110, <https://doi.org/10.1785/0220220022>, 2022.
- Ren, Z. Y., Zhao, X., and Liu, H.: Dispersion Effects on Tsunami Propagation in South China Sea, *Journal of Earthquake and Tsunami*, 9, <https://doi.org/10.1142/S1793431115400011>, 2015.
- Rockwell, T. K. and Ben-Zion, Y.: High localization of primary slip zones in large earthquakes from paleoseismic trenches: Observations and implications for earthquake physics, *Journal of Geophysical Research: Solid Earth*, 112, 10 304, <https://doi.org/10.1029/2006JB004764>, 2007.
- 705 Rogers, T. H. and Nason, R. D.: Active displacement on the Calaveras fault zone at Hollister, California, *Bulletin of the Seismological Society of America*, 61, 399–416, 1971.
- Ruiz-Angulo, A., Jónsdóttir, K., Prastarson, R. H., Halldórsson, B., Drouin, V., Grímsdóttir, H., and Jónsson, S.: Preliminary Simulations for Tsunami Hazard in Connection with a major Earthquake on the Húsavík-Flatey Fault, in: *Proceedings of the Northquake 2019 workshop* (Ed. S. Jónsson et al.), pp. 54–60, Húsavík Academic Centre, 2019.
- 710 Ryan, W. B., Carbotte, S. M., Coplan, J. O., O’Hara, S., Melkonian, A., Arko, R., Weissel, R. A., Ferrini, V., Goodwillie, A., Nitsche, F., Bonczkowski, J., and Zemsky, R.: Global Multi-Resolution Topography synthesis, *Geochemistry, Geophysics, Geosystems*, 10, <https://doi.org/10.1029/2008GC002332>, 2009.
- 715 Sæmundsson, K.: Evolution of the Axial Rifting Zone in Northern Iceland and the Tjörnes Fracture Zone, *GSA Bulletin*, 85, 495–504, [https://doi.org/https://doi.org/10.1130/0016-7606\(1974\)85<495:EOTARZ>2.0.CO;2](https://doi.org/https://doi.org/10.1130/0016-7606(1974)85<495:EOTARZ>2.0.CO;2), 1974.
- Schliwa, N. and Gabriel, A.-A.: Fault damage zone effects on near-field ground motion parameters and plastic strain in a multi-scale dynamic rupture model of the 2019 Ridgecrest sequence, in: *Poster Presentation at 2022 SCEC Annual Meeting*, edited by Schliwa, N. and Gabriel, A.-A., <https://www.scec.org/publication/12443>, 2022.
- 720 Scicchitano, G., Gambino, S., Scardino, G., Barreca, G., Gross, F., Mastronuzzi, G., and Monaco, C.: The enigmatic 1693 AD tsunami in the eastern Mediterranean Sea: new insights on the triggering mechanisms and propagation dynamics, *Scientific Reports*, 12, 1–23, <https://doi.org/10.1038/s41598-022-13538-x>, 2022.
- 725 Selva, J., Lorito, S., Volpe, M., Romano, F., Tonini, R., Perfetti, P., Bernardi, F., Taroni, M., Scala, A., Babeyko, A., Løvholt, F., Gibbons, S. J., Macías, J., Castro, M. J., González-Vida, J. M., Sánchez-Linares, C., Bayraktar, H. B., Basili, R., Maesano, F. E., Tiberti, M. M., Mele, F., Piatanesi, A., and Amato, A.: Probabilistic tsunami forecasting for early warning, *Nature Communications*, 12, 1–14, <https://doi.org/10.1038/s41467-021-25815-w>, 2021.



- Seno, T. and Hirata, K.: Did the 2004 Sumatra–Andaman Earthquake Involve a Component of Tsunami Earthquakes?, *Bulletin of the Seismological Society of America*, 97, S296–S306, <https://doi.org/10.1785/0120050615>, 2007.
- Socquet, A., Hollingsworth, J., Pathier, E., and Bouchon, M.: Evidence of supershear during the 2018 magnitude 7.5 Palu earthquake from space geodesy, *Nature Geoscience*, 12, 192–199, <https://doi.org/10.1038/s41561-018-0296-0>, 2019.
- 730 Sperner, B., Müller, B., Heidbach, O., Delvaux, D., Reinecker, J., and Fuchs, K.: Tectonic stress in the Earth’s crust: advances in the World Stress Map project, *Geological Society Special Publication*, 212, 101–116, <https://doi.org/10.1144/GSL.SP.2003.212.01.07>, 2003.
- Stefansson, R., Gudmundsson, G. B., and Halldorsson, P.: Tjörnes fracture zone. New and old seismic evidences for the link between the North Iceland rift zone and the Mid-Atlantic ridge, *Tectonophysics*, 447, 117–126, <https://doi.org/10.1016/J.TECTO.2006.09.019>, 2008.
- 735 Tanioka, Y. and Satake, K.: Tsunami generation by horizontal displacement of ocean bottom, *Geophysical Research Letters*, 23, 861–864, <https://doi.org/https://doi.org/10.1029/96GL00736>, 1996.
- Taufiqurrahman, T., Gabriel, A.-A., Ulrich, T., Valentová, L., Gallovič, F., and Gabriel, A.-A.: Broadband dynamic rupture modeling with fractal fault roughness, frictional heterogeneity, viscoelasticity and topography: The 2016 Mw 6.2 Amatrice, Italy earthquake, *Geophysical Research Letters*, p. e2022GL098872, <https://doi.org/10.1029/2022GL098872>, 2022.
- 740 Taufiqurrahman, T., Gabriel, A.-A., Li, D., Ulrich, T., Li, B., Carena, S., Verdecchia, A., and Gallovič, F.: Dynamics, interactions and delays of the 2019 Ridgecrest rupture sequence, *Nature*, pp. 1–8, <https://doi.org/10.1038/s41586-023-05985-x>, 2023.
- Torsvik, T. H., Amundsen, H. E., Trønnes, R. G., Doubrovine, P. V., Gaina, C., Kuszniir, N. J., Steinberger, B., Corfu, F., Ashwal, L. D., Griffin, W. L., Werner, S. C., and Jamtveit, B.: Continental crust beneath southeast Iceland, *Proceedings of the National Academy of Sciences of the United States of America*, 112, E1818–E1827, <https://doi.org/10.1073/pnas.1423099112>, 2015.
- 745 Tsai, V. C., Ampuero, J.-P., Kanamori, H., Stevenson, D. J., Tsai, V. C., Ampuero, J.-P., Kanamori, H., and Stevenson, D. J.: Estimating the effect of Earth elasticity and variable water density on tsunami speeds, *Geophysical Research Letters*, 40, 492–496, <https://doi.org/10.1002/GRL.50147>, 2013.
- Uieda, L., Tian, D., Leong, W. J., Jones, M., Schlitzer, W., Grund, M., Toney, L., Yao, J., Magen, Y., Materna, K., Newton, T., Anant, A., Ziebarth, M., Quinn, J., and Wessel, P.: PyGMT: A Python interface for the Generic Mapping Tools, *Zenodo*, <https://doi.org/10.5281/zenodo.6702566>, 2022.
- 750 Ulrich, T., Gabriel, A. A., Ampuero, J. P., and Xu, W.: Dynamic viability of the 2016 Mw 7.8 Kaikōura earthquake cascade on weak crustal faults, *Nature Communications*, 10, <https://doi.org/10.1038/s41467-019-09125-w>, 2019a.
- Ulrich, T., Vater, S., Madden, E. H., Behrens, J., van Dinther, Y., van Zelst, I., Fielding, E. J., Liang, C., and Gabriel, A. A.: Coupled, Physics-Based Modeling Reveals Earthquake Displacements are Critical to the 2018 Palu, Sulawesi Tsunami, *Pure and Applied Geophysics*, 176, 4069–4109, <https://doi.org/10.1007/s00024-019-02290-5>, 2019b.
- 755 Ulrich, T., Gabriel, A. A., and Madden, E. H.: Stress, rigidity and sediment strength control megathrust earthquake and tsunami dynamics, *Nature Geoscience*, 15, 67–73, <https://doi.org/10.1038/s41561-021-00863-5>, 2022.
- Uphoff, C., Rettenberger, S., Bader, M., Madden, E. H., Ulrich, T., Wollherr, S., and Gabriel, A.-A.: Extreme Scale Multi-Physics Simulations of the Tsunamiogenic 2004 Sumatra Megathrust Earthquake, *Proceedings of the International Conference for High Performance Computing, Networking, Storage and Analysis SC17*, <https://doi.org/10.1145/3126908.3126948>, 2017.
- 760 van Zelst, I., Rannabauer, L., Gabriel, A. A., and van Dinther, Y.: Earthquake Rupture on Multiple Splay Faults and Its Effect on Tsunamis, *Journal of Geophysical Research: Solid Earth*, 127, e2022JB024 300, <https://doi.org/10.1029/2022JB024300>, 2022.
- Wang, K. and Dixon, T.: “Coupling” Semantics and science in earthquake research, *Eos, Transactions American Geophysical Union*, 85, 180, <https://doi.org/https://doi.org/10.1029/2004EO180005>, 2004.



- 765 Wessel, P., Luis, J. F., Uieda, L., Scharroo, R., Wobbe, F., Smith, W. H., and Tian, D.: The Generic Mapping Tools Version 6, *Geochemistry, Geophysics, Geosystems*, 20, 5556–5564, <https://doi.org/10.1029/2019GC008515>, 2019.
- Wilson, A. and Ma, S.: Wedge Plasticity and Fully Coupled Simulations of Dynamic Rupture and Tsunami in the Cascadia Subduction Zone, *Journal of Geophysical Research: Solid Earth*, 126, e2020JB021 627, <https://doi.org/10.1029/2020JB021627>, 2021.
- Wirp, A. S., Gabriel, A. A., Schmeller, M., H. Madden, E., van Zelst, I., Krenz, L., van Dinther, Y., and Rannabauer, L.: 3D Linked Sub-  
770 duction, Dynamic Rupture, Tsunami, and Inundation Modeling: Dynamic Effects of Supershear and Tsunami Earthquakes, Hypocenter Location, and Shallow Fault Slip, *Frontiers in Earth Science*, 9, 177, <https://doi.org/10.3389/feart.2021.626844>, 2021.
- Wollherr, S., Gabriel, A.-A., and Uphoff, C.: Off-fault plasticity in three-dimensional dynamic rupture simulations using a modal Discontinuous Galerkin method on unstructured meshes: implementation, verification and application, *Geophysical Journal International*, 214, 1556–1584, <https://mediatum.ub.tum.de/doc/1525762/1525762.pdf>, 2018.
- 775 Wollherr, S., Gabriel, A. A., and Mai, P. M.: Landers 1992 “Reloaded”: Integrative Dynamic Earthquake Rupture Modeling, *Journal of Geophysical Research: Solid Earth*, 124, 6666–6702, <https://doi.org/10.1029/2018JB016355>, 2019.
- Yamamoto, T.: Gravity waves and acoustic waves generated by submarine earthquakes, *International Journal of Soil Dynamics and Earthquake Engineering*, 1, 75–82, [https://doi.org/10.1016/0261-7277\(82\)90016-X](https://doi.org/10.1016/0261-7277(82)90016-X), 1982.
- Ziegler, M., Rajabi, M., Heidbach, O., Hersir, G. P., Ágústsson, K., Árnadóttir, S., and Zang, A.: The stress pattern of Iceland, *Tectonophysics*,  
780 674, 101–113, <https://doi.org/10.1016/J.TECTO.2016.02.008>, 2016.
- Zoback, M. L.: First- and second-order patterns of stress in the lithosphere: The World Stress Map Project, *Journal of Geophysical Research: Solid Earth*, 97, 11 703–11 728, <https://doi.org/10.1029/92JB00132>, 1992.
- Zoback, M. L., Zoback, M. D., Adams, J., Assumpção, M., Bell, S., Bergman, E. A., Blümling, P., Brereton, N. R., Denham, D., Ding, J., Fuchs, K., Gay, N., Gregersen, S., Gupta, H. K., Gvishiani, A., Jacob, K., Klein, R., Knoll, P., Magee, M., Mercier, J. L., Müller, B. C.,  
785 Paquin, C., Rajendran, K., Stephansson, O., Suarez, G., Suter, M., Udias, A., Xu, Z. H., and Zhizhin, M.: Global patterns of tectonic stress, *Nature*, 341, 291–298, <https://doi.org/10.1038/341291a0>, 1989.
- Þorgeirsson, O.: Sögulegir jarðskjálftar á Norðurlandi (Historic earthquakes in Northern Iceland), in: *Proceedings of a workshop in Husavik, North Iceland, Þekkingarnet Þingeyinga*, <https://hac.is/sogulegir-jardskjalftar-a-nordurlandi>, 2011.